



Title	Electrical spin injection from ferromagnet into an InAs quantum well
Author(s)	石倉, 文継
Citation	北海道大学. 博士(工学) 甲第11753号
Issue Date	2015-03-25
DOI	10.14943/doctoral.k11753
Doc URL	http://hdl.handle.net/2115/58800
Type	theses (doctoral)
File Information	Tomotsugu_Ishikura.pdf



[Instructions for use](#)

**Electrical spin injection from ferromagnet
into an InAs quantum well**

by

Tomotsugu Ishikura

A dissertation

**submitted in partial fulfillment of the requirements
for the degree of Doctor of Philosophy**

**Graduate School of Information Science and Technology,
Hokkaido University**

© Copyright by Tomotsugu Ishikura

2015. All Right Reserved.

Acknowledgements

This dissertation describes a research work carried out at Research Center for Integrated Quantum electronics (RCIQE) while the author was a graduate student at Graduate School of Information Science and Technology, Hokkaido University from 2010 to 2015. From 2010 to 2013 author was under the supervision of past Professor Kanji Yoh by when he was deceased in October, 2013. Subsequently, Associate professor Tetsuya Uemura supervised this work from 2014 to 2015.

First and foremost, I sincerely appreciate my parents and brothers for their constant support and encouragement. I would like to extend my sincere gratitude to my past supervisor Professor Kanji Yoh for his support and encouragement throughout my graduate study. This thesis would not have been accomplished without him. You are one of the most passionate researcher I have worked with. I learned a lot of things form you during four years both on scientific and personal level. You were always available for discussion and helping me even when you struggled with his serious illness. I am thankful and respectful towards your patience and attitudes for work.

I am also great pleasure for me to express my sincere gratitude and indebtedness to my recent supervisor Associate professor Tetsuya Uemura. You accepted to become my supervisor after Professor Yoh was gone. During only one year, I have learned so many things from you thorough discussion on the aspects of spintronics and approach to my work. You were always helpful and your great advices guide me to solve a lot of problems for acquiring my PhD. degree.

I am grateful to my committee members, Professor Masafumi Yamamoto, Professor Seiya Kasai, and Associate professor Taketomo Sato, for devoting their time to review this dissertation and providing valuable suggestions and comment to improve the quality of this dissertation.

I would like to acknowledge my collaborators who contributed to this thesis. I express special thanks to Zhixin Cui, Dr. Keita Konishi, and Dr. Takashi Matsuda at my laboratory for their technical support and contributions to the InAs spin based device process and

measurement technique. My gratitude is extended to Lennart –Knud Liefeyth and Professor Wolfgang Hansen at Institut für Angewandte Physik und Zentrum für Mikrostrukturforschung, Hamburg University in Germany for their discussion and analysis.

I would like to express my appreciation to Professor Takashi Fukui, Professor Tamotsu Hashizume, Professor Eiichi Sano, and Professor Junichi Motohisa, Professor Ikuo Suemune, Professor Kazuhisa Sueoka, Associate professor Masamichi Akazawa, Associate professor Shinjiroh Hara and Dr. Agus Subagyo for guidance and improvement of well-founded high interdisciplinary environment of RCIQE and Graduate School of Information Science and Technology.

I would like to spend invaluable time with Yoh's Group, Dr, Bubesh Babu, Dr. Rajagembu Perumal, Dr. Joungeob Lee, Dr. Takashi Matsuda, Dr. Keita Konishi, Takeshi Ejiri, Kenji Suzuki, Zhixin Cui, Liumin Zou, Yan Ziwei, Takahiro Hiraki, and Takao Miyamoto.

I would like to thank every RCIQE group members for constant support and encouragement.

Contents

Chapter 1	Introduction	1
1.1	Motivation	2
1.2	Objective	4
1.3	Outline	5
	Bibliography	7
Chapter 2	Spin injection, detection and transport	9
2.1	Spin injection and transport in non-ferromagnet	9
2.1.1	Conductivity mismatch	10
2.1.2	Spin injection through interfacial tunneling barrier	13
2.2	Spin transport in semiconductor	16
2.2.1	Spin relaxation	16
2.2.2	Structural Inversion asymmetry	20
2.2.3	Bulk inversion asymmetry	22
2.3	Spin injection and detection measurement	24
2.3.1	Two-terminal local geometry	24
2.3.2	Four-terminal nonlocal geometry	26
2.3.3	Hanle effect measurement	28
2.4	Spin FET	29
2.4.1	Spin FET in two-dimensional system	30
	Bibliography	32
Chapter 3	Experimental methods	33
3.1	Sample fabrication	33
3.1.1	Gated Hall-bar	33
3.1.2	Lateral spin valves	34
3.2	Electrical measurement in an InAs quantum well	37

3.2.1 Shubnikov-de Haas oscillation -----	37
Chapter 4 Thermal stability of Pd gate in pseudomorphic InGaAs	
heterostructures -----	39
4.1 Introduction -----	39
4.2 InP HEMT structure-----	40
4.3 Result and discussion -----	42
Bibliography -----	47
Chapter 5 Spin injection into InAs quantum well -----	49
5.1 InAs quantum well structure -----	49
5.2 Spin injection into n-Si -----	51
5.2.2 Spin valve measurement in NiFe/MgO/n-Si-----	52
5.2.3 Hanle effect measurement in NiFe/n-Si-----	55
5.3 Spin injection into InAs quantum well -----	58
5.3.1 Device structure-----	58
5.3.2 Electrical characteristics in NiFe/MgO/InAs-----	59
5.3.4 Spin valve measurement-----	60
5.3.5 Hanle effect measurement-----	65
5.4 Anomalous Hall signals by out-of plane spin injection from ferromagnet into an InAs	
quantum well -----	68
5.4.1 Device structure -----	68
5.4.2 Result and discussion -----	71
5.4.3 Conclusion -----	73
Bibliography -----	74
Chapter 6 Summary of dissertation-----	77
List of Publication and conference	

List of Figures

1.1	Schematic of the Datta-Das spin-FET -----	3
2.1.1	Dependence of $\Delta R/R_P$ on σ_{NM}/σ_{FM} -----	12
2.1.2	Logarithm scale for dependence of $\Delta R/R_P$ on σ_{NM}/σ_{FM} -----	12
2.1.3	The magnetoresistance versus contact resistivity in InAs QW and grapheme -	6
2.2.1	Illustration of the Elliot-Yafet spin relaxation mechanism -----	19
2.2.2	Illustration of the D'yakonov-Perel' mechanism -----	20
2.2.3	Illustration of the degenerated spin split band in narrow gap QW, the energy dispersion relation to k-space, and effective magnetic field of SIA -----	22
2.2.4	Illustration of the effective magnetic field due to linear BIA -----	23
2.3.1	Schematics of the two terminal local spin valve configuration and ideal spin valve signals -----	25
2.3.2	Schematics of the four-terminal non-local spin valve configuration and ideal spin valve signals -----	27
2.3.3	Schematics of the Hanle effect measurement -----	29
2.4.1	Spin precession and non-precession configuration in 1-D InAs QW -----	30
3.1	A fabricated lateral spin valve device picture -----	37
3.2.1	The Shubnikov-de Haas oscillation in weak spin orbit interaction -----	39
3.2.2	The Shubnikov-de Haas oscillation in strong spin orbit interaction -----	39
4.1	Schematic heterostructure diagram of the InGaAs-based HEMT transistor --	42
4.2	A fabricated Hall bars -----	42
4.3	A schematic of conduction diagram of the Schottky junction -----	43
4.4	Drain and gate current characteristics of one of the fabricated devices -----	43
4.5	A Schottky diode characteristics of the device -----	44
4.6	Threshold voltage shift (a), Schottky barrier height shift (b), and Ideality factor shift (c) are illustrated as function of annealing temperature -----	44
4.7	The Schottky barrier height and ideality factor dependant on annealing temperature -----	46
5.1.1	Layer and band structures of InGaAs-based heterostructure -----	50

5.1.2	Electrical transfer characteristics and SOI strength data -----	51
5.2.1	Schematics of fabricated nonlocal lateral spin valves in n-Si -----	52
5.2.2a	Result of a nonlocal spin injection (NiFe/MgO/n-Si) at 1.4 K -----	53
5.2.2b	Spatial FM electrodes dependence of nonlocal voltage at 1.4 K -----	54
5.2.2c	Bias dependence of nonlocal voltage at 1.4 K for L=1.4 μ m sample -----	54
5.2.3	Schematic of the three terminal Hanle configuration in Fe/n-Si -----	55
5.2.4	Result of three terminal Hanle measurement in Fe/n-Si at 1.4 K -----	56
5.2.5	The narrower peaks were shown in $I=\pm 0.5$ and ± 3 mA including the fitting of Lorentzian function -----	57
5.2.6	Three-terminal Hanle amplitude as a function of biased current -----	57
5.3.2	RA-voltage characteristics in the NiFe/MgO/InAs QW at RT and 1.4 K -----	60
5.3.3	Non-local spin-valve signals and three terminal measurement in NiFe/MgO/InAs and NiFe/InAs structures -----	62
5.3.4	Magnitude of nonlocal spin-valve signal for NiFe/MgO/InAs as a function of spacing between ferromagnetic electrodes -----	66
5.3.5	ΔRNL versus spin resistance mismatch -----	65
5.3.6	The Hanle effect measurement in NiFe/MgO/InAs QW -----	67
5.4.1	Schematic diagram of the InAs heterostructure -----	69
5.4.2	Quantum Hall effect and Shubnikov-de Haas oscillations in 1.5 K -----	69
5.4.3	Optical microscopy image of the device -----	70
5.4.4	Conventional Hall measurement result was obtained at room temperature ---	71
5.4.5	Schematic diagram of the Hall-device with Ferromagnetic electrode on InAs inverted heterostructure -----	72
5.4.6	Hall voltage measurement in the absence of external magnetic field -----	72

Chapter 1

Introduction

Size of silicon based metal-oxide-semiconductor field effect transistor (MOSFET) has been recently reached to the order of 10 nm for advance of information processing performance. However, it is hard to continue the scaling down the transistor size because of physical limitation as regarding to device process and design. The device process have mainly trouble about development difficulty for shorter-wavelength light of optical lithography beyond ArF laser. While, sub-threshold leakage due to the scaling down is another issue for device design. However, double patterning and three-dimensional structure technologies were used as temporary solutions, it is only a matter of time before the developments stop. Thus, this fundamental obstacle requires an alternative new materials and functional devices. Spintronics is expected for one of the most promising solutions for overcome these obstacles. This field is motivated that spin degree of freedom is applied for electronic devices [1].

The emergence of spintronics originated from discovery of giant magnetoresistance (GMR) effect by P. Grünberg and A. Fert in 1987. So far, the technology has contributed to magnetic head in hard disk drive (HDD) and magnetic random access memories (MRAM). Besides that, spin-based device as transistor is also great concerned as represented by spin field effect transistor (spin FET). The spin FET was first proposed by S. Datta and B. Das in 1990 [2]. The new device has possibility to achieve better switching performance than the conventional MOSFET. The spin FET operation is based on the technology both spin injection/detection and manipulation,

however, it has not been confirmed yet due to obstacles with spin creation and manipulation in semiconductors (SCs).

1.1 Motivation

The concept of spin-FET is electrical resistance modulation by gate control of electric field as magnetic force without external magnetic field. The spin FET has ferromagnetic electrodes for source and drain, which is used for spin injector and detector as shown in Fig. 1.1. The channel consists of narrow gap semiconductors based two dimensional electron gas because these have strong spin orbit coupling (e.g. InGaAs, InAs, InSb). The spin orbit coupling enables to manipulate the spin precession frequency of conducted spin in the quantum well. It takes a strong magnetic force that interacts to conducted spin. The magnetic force makes the spin precession in the center of spin orbit coupling orientation (channel width orientation). The spin precession angles at the ferromagnetic detector are expressed with channel length L and strength of spin orbit coupling $\alpha(V_g)$ as described below.

$$\Delta\theta = \frac{2\alpha(V_g)m^*L}{\hbar^2} \quad (1.1.1)$$

where m^* is the effective mass. If the gate electric field is adjusted to precession angle at the detector by 180 degree, the spin angle will be anti-parallel to magnetized orientation of detector, and so the spin will be reflected by the drain. If the angle is 0 (or 360) degree, the spin will get thorough. Thus, the Datta-Das type spin FET is analogue to a conventional MOSFET without control of spin precession. The energy consumes for switching in the spin FET is apparently much less than the conventional MOSFET, since the small energy is used as switching motion.

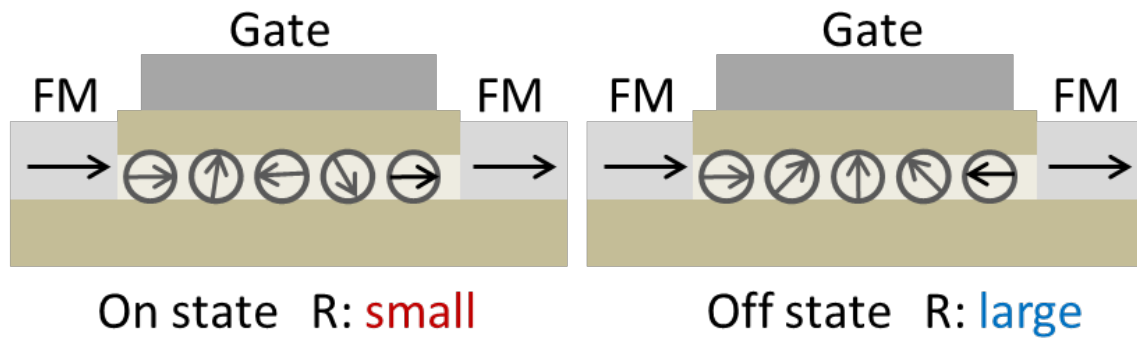


Figure 1.1 Schematic of the Datta-Das spin-FET

To enhance the spin FET performance, strong spin orbit interaction and highly efficient spin injection/detection is crucial. The strong spin orbit interaction make it possible to decrease the channel length, because it needs to be hold longer than spin precession length which is the distance during the spin precession angle change from 0 to 180 degree. It was reported that the enhancement of the spin orbit interaction have been reported by adjustment of layer structure [3-7], 2-dimensional electron gas (2DEG) based quantum wire [8-9] and nanowire [10-13]. However, the spin precession length needs to be much shorter for device application, as considered to the minimum length of 70 nm in previous reports [14]. In addition, the spin injection/detection from ferromagnet into semiconductors is another issue. So far, the spin injection/detection experiment have been demonstrated by using both optical and electrical detection method as represented to spin light emitting diode (LED) [15-17] and nonlocal spin accumulation geometry [18-24], respectively. The conductivity mismatch is an obstacle that decreases the spin injection efficiency in the FM/SC interface [25]. This obstacles can be overcome by inserted a Schottky barrier or a tunneling barrier in FM/SC junction as it has been reported that optimized control of the junction resistance plays a crucial role in enabling efficient spin injection and detection [26]. There have been many reports on spin injection into highly doped bulk layer of GaAs [18-19], Si [20] or Ge [21] using a FM/SC Schottky tunnel barrier or an FM/insulator/SC tunnel barrier. On the other hands, there have been very few reports on the nonlocal detection of spin injection into narrow-gap semiconductors. These have been limited to

CoFe/In_{0.75}Ga_{0.25}As [22] or NiFe/In_{0.53}Ga_{0.47}As/InAs quantum well (QW) [23] structures with an FM/InGaAs Schottky tunnel barrier, and the reported spin injection efficiency of these materials is relatively low compared to other materials. A possible origin of the relatively low spin injection efficiency in FM/InGaAs heterojunctions is low tunnel resistance due to a low Schottky barrier height of the FM/InGaAs heterojunction, resulting in a conductivity mismatch. Thus, insertion of a tunneling barrier between the ferromagnet and semiconductor is necessary to achieve highly efficient spin injection into narrow gap semiconductors.

1.2 Objective

This dissertation aim to that highly efficient spin injection and detection from ferrmagnet into an InAs quantum well. Especially, the spin injection from NiFe spin injector into an InAs quantum well through an MgO tunneling barrier is investigated. With a secondary theme, thermal stability of Pd gate on InAlAs is evaluated for a solution against gate deterioration during thermal treatment in a spin FET process.

1.2 Outline

This dissertation mainly focuses on spin injection and detection in InAs quantum well in the purpose of realization for spin based semiconductor devices. The evaluation of gate material on InAlAs is also investigated to optimize the process with a secondly theme.

In chapter 2, the theory regarding spin injection, detection and transport mechanism is introduced. The fundamental obstacle with spin injection into non-ferromagnet, as called conductivity mismatch, is focused. Then, the tunneling barrier playing roll for suppress the conductivity mismatch problem are described.

In chapter 3, an overview of the device process technique and flow is described.

In chapter 4, thermal stability of Pd gate on InAlAs is described. Since Ni and Fe as the ferromagnet electrode is easy to diffusive the InAs around 120 °C, and then thermal treatment deteriorate the gate characteristics. On the other hands, generally used Ti/Au and Ti/Pt/Au gates on InAlAs are also poor with resistance against thermal treatment over 200 °C. The deterioration of gate characteristics during thermal treatment required process, such like a resist bake, make a problem for spin FET process. Thus, Pd/InAlAs Schottky gate was evaluated in regard to thermal stability over 200 °C. The analysis of a fabricated Pd/InAlAs gated FET was conducted by using voltage-current measurements.

In chapter 5, spin injection and detection in semiconductor is described. First, NiFe/MgO/n-Si and Fe/n-Si non-local spin valves were fabricated for confirming the tunneling barrier effectiveness. The NiFe/MgO/n-Si sample show clear spin valve signals due to interface resistance adjustment, but any nonlocal signals was not shown in Fe/n-Si case. It seemed that the signal of Fe/n-Si was too low to detect in nonlocal configuration. To analyze it further, three-terminal Hanle effect measurement was conducted, which make it possible to detect the spin accumulation without spin relaxation in channel. The Hanle effect measurement result showed a clear spin accumulation and another effect signals simultaneously. The origin of another effect is discussed in aspect of bias voltage dependence of the Hanle amplitude. Based on these

results, spin injection into InAs quantum well through MgO tunnel barrier was conducted. The spin accumulation signal was observed in the fabricated NiFe/MgO/InAs nonlocal spin valves, and then spin-related parameters were evaluated. The spin polarization in InAs quantum well reached to 9 % and the value was 4 times higher than the previous reported value of NiFe/InGaAs/InAs. It is possible to realize that the further study will perform a highly efficient spin injection into InAs quantum well. Finally, the nuclear spin polarization in InAs quantum well was challenged. An anomalous Hall effect signal was detected when spin was injected from ferromagnet as source electrode in Hall-bar. The anomalous signals probably indicated to nuclear spin polarization in InAs quantum well by spin injection from analysis of the signal amplitude.

Finally, chapter 6 provides a summary of this dissertation.

Bibliography

- [1] I. Zutic, J. Fabian and S. Das Sarma, *Rev. Mod. Phys.* 76, 323 (2004).
- [2] S. Datta and B. Das, *Appl. Phys. Lett.* 56, 665 (1990).
- [3] P. Pfeffer and W. Zawadzki, *Phys. Rev. B* 52, R144332 (1995).
- [4] T. Matsuda and K. Yoh, *J. Electron. Mater.* 37, 1806 (2008).
- [5] E.A. de Andrada e Silva, G.C. La Rocca and F. Bassani, *Phys. Rev. B* 55, 16293 (1997).
- [6] Y. Sato, T. Kita, S. Gozu, and S. Yamada, *J. Appl. Phys.* 89, 8017 (2001).
- [7] H. Choi, T. Kakegawa, M. Akabori, T. Suzuki, and S. Yamada, *Physica E* 40, 2823 (2008).
- [8] T. Schapers, J. Knobbe, V. A. Guzenko, *Phys. Rev. B* 69, 135323 (2004).
- [9] C. H. L. Quay, T. L. Hughes, J. A. Sulpizio, L. N. Pfeiffer, K. W. Baldwin, K. W. West, D. Gordon and R. de Picciotto, *Nat. Phys.* 6, 336 (2010).
- [10] D. Liang and X. P. A. Gao, *Nano letter* 12, 3263 (2012)
- [11] A. Bringer and Th. Schapers, *Phys. Rev. B* 83, 115305 (2011).
- [12] A. E. Hansen, M. T. Bjork, I. C. Fasth, C. Thelander and L. Samuelson, *Phys. Rev. B* 71, 205328 (2005).
- [13] P. Roulleau, T. Choi, S. Riedi, T. Heinzl, I. Shorubalko, T. Ihn and K. Ensslin, *Phys. Rev. B* 81, 155449 (2010).
- [14] T. Matsuda and K. Yoh, *Physica E* 42, 979 (2010).
- [15] Y. Ohno, D. K. Young, B. Beschoten, F. Matsukura, H. Ohno and D. D. Awschalom, *Nature* 402, 790 (1999).
- [16] H. J. Zhu, M. Ramsteiner, H. Kostial, M. Wassermeier, H. P. Schonherr, and K. H. Ploog, *Phys. Rev. Lett.* 87, 016601 (2001).
- [17] K. Yoh, H. Ohno, K. Sueoka, and M. E. Ramsteiner, *J. Vac. Sci. Technol. B* 22, 1432 (2004)
- [18] X. Lou, C. Adelman, S. A. Crooker, E. S. Garlid, J. Zhang, K. S. M. Reddy, S. D. Flexner, C. J. Palmstrom and P. A. Crowell, *Nature Physics* 31, 197 (2007).
- [19] T. Uemura, T. Akiho, M. Harada, K. -i. Matsuda and M. Yamamoto, *Appl. Phys.*

- Lett. 99, 082108 (2011).
- [20] T. Sasaki, T. Oikawa, T. Suzuki, M. Shiraishi, Y. Suzuki, and K. Tagami, Appl. Phys. Express 2, 053003 (2009).
- [21] Y. Zhou, W. Han, L. -T. Chang, F. Xiu, M. Wang, M. Oehme, I. A. Fischer, J. Schulze, R. K. Kawakami, and K. L. Wang, Phys. Rev. B 84, 125323 (2011).
- [22] S. Hidaka, M. Akabori and S. Yamada, Appl. Phys. Express 5, 113001 (2012).
- [23] H. C. Koo, H. Yi, J. B. Ko, J. Chang, S. H Han, D. Jung, S. G. Huh and J. Eom, Appl. Phys. Lett. 90, 022101 (2007).
- [24] K. Konishi, Z. Cui, T. Hiraki and K. Yoh, J. of Crys. Grow. 378, 385 (2013).
- [25] G. Schmidt, D. Ferrand, L. W. Mollenkamp, A. T. Phillip and B. J. van Wees, Phys. Rev. B 62, R4790 (2000).
- [26] A. Fert and H. Jaffr es, Phys. Rev. B 64, 184420 (2001).

Chapter 2

Spin injection, detection and transport

2.1 Spin injection and transport in non-ferromagnet

This section focus on the spin injection and accumulation in non-ferromagnet. The fist experimental demonstration was conducted by Johonson and Silsbee. [1] In the density of state (DOS) of spin polarization inside ferromanget play roll which is observation of spin injection and detection in non-ferromagnet. The spin injection into non-ferromagnet from ferromagnet induces to spin accumulation in the non-ferromagnet. As considered to current flow between ferromagnet and non-ferromagnet, the conductivity of spin-up and spin-down is not accorded, as called a spin current ($I_{\uparrow} - I_{\downarrow}$).

$$j_{\uparrow\downarrow} = \frac{\sigma_{\uparrow\downarrow}}{e} \frac{\partial \mu_{\uparrow\downarrow}}{\partial x} \quad (2.1.1)$$

where $j_{\uparrow\downarrow}$ is the spin up (spin down) current density. The spin current accompany with a charge current simultaneously. Then, the injected spin make the non-ferromagnet magnetized caused by the spin accumulation. It is related to the difference of population spin-up and spin-down as expressed by chemical potential ($\mu_{\uparrow} - \mu_{\downarrow}$). The spin dependent conductivity form as according to Einstein relation

$$\sigma_{\uparrow\downarrow} = e^2 N_{\uparrow\downarrow}(E_F) D_{\uparrow\downarrow} \quad (2.1.2)$$

where $\sigma_{\uparrow\downarrow}$ is the spin dependent conductivity, and $N(E_F)$ is the density of state in

Fermi energy and $D_{\uparrow\downarrow}$ is the diffusion constant. Then, $D_{\uparrow\downarrow}$ is given by $D = 1/3v_{F\uparrow\downarrow}l_{\uparrow\downarrow}$ where $v_{F\uparrow\downarrow}$ is the Fermi velocity and $l_{\uparrow\downarrow}$ is the spin dependent electron mean free path. The spin polarization ratio comes from spin dependent conductivity asymmetry which can be formed as

$$\alpha = \frac{j_{\uparrow} - j_{\downarrow}}{j_{\uparrow} + j_{\downarrow}} \quad (2.1.3)$$

It assumes that conducted spin is limited to one dimensional diffusion. By using the spin averaged diffusion constant $D = D_{\uparrow}D_{\downarrow}(N_{\uparrow} + N_{\downarrow})/(D_{\uparrow}N_{\uparrow} + D_{\downarrow}N_{\downarrow})$ and τ_{sf} is the spin relaxation time, Einstein relation transform to

$$D \frac{\partial^2(\mu_{\uparrow} - \mu_{\downarrow})}{\partial x^2} = \frac{(\mu_{\uparrow} - \mu_{\downarrow})}{\tau_{sf}} \quad (2.1.4)$$

Finally, the general solution of the equation is given by:

$$\mu_{\uparrow\downarrow} = A + Bx + \frac{C}{\sigma_{\uparrow\downarrow}} \exp\left(-\frac{x}{\lambda_{sf}}\right) + \frac{D}{\sigma_{\uparrow\downarrow}} \exp\left(\frac{x}{\lambda_{sf}}\right) \quad (2.1.5)$$

where A, B, C and D are defined in boundary condition between ferromagnet and non-ferromagnet and λ_{sf} is the spin diffusion length which is expressed as $\lambda_{sf} = \sqrt{D\tau_{sf}}$. The boundary conditions in ferromagnet/non-ferromagnet interface are first explained by Schmidt theory, which is considered to chemical potential continuity at the interface. While, Fert expanded the theory to be general condition in regard to chemical potential discontinuity. These details are explained as follows.

2.1.1 Conductivity mismatch

Schmidt et al predicted the obstacles for efficient spin injection into semiconductors in 2000 as called conductivity mismatch. [2] In this section, the efficiency of spin injection into non-ferromagnet from ferromagnet is explained. In situation of the interface resistance and spin relaxation at the interface are neglected, the spin dependent chemical potential continues crossover the interface. The electrical chemical potentials exponentially decay with the length inside non-ferromagnet resulted to $\mu_{\uparrow}(\pm\infty) = \mu_{\downarrow}(\pm\infty)$. As considered to the boundary condition at the injector and detector, detectable magnetoresistance signal is expressed by

$$\frac{\Delta R}{R_P} = \frac{\beta^2}{1 - \beta^2} \left(\frac{\lambda_{FM} \sigma_{NM}}{\sigma_{FM} x} \right)^2 \frac{4}{\left(2 \frac{\lambda_{FM} \sigma_{NM}}{x \sigma_{FM}} + 1 \right)^2 - \beta^2} \quad (2.1.6)$$

where R_P is the resistance in ferromagnets magnetized in parallel, β is the spin polarization in ferromagnet, λ_{FM} is the spin diffusion length of ferromagnet, $\sigma_{FM(NM)}$ is the conductivity of ferromagnet (non-ferromagnet). In sandwich of ferromagnet, the equation is shortening to:

$$\frac{\Delta R}{R} = \frac{\beta^2}{(\beta - 1)(\beta + 1)} \quad (2.1.7)$$

As considered that the β is limited to be less than 100% and short spin diffusion length of ferromagnet ~ 10 nm, This equation 2.3.6 shows that the observable magnetoresistance is completely dominated by the ratio of conductivities in non-ferromagnet and ferromagnet σ_{NM}/σ_{FM} . Figure 2.3.1 and 2.3.2 indicate that the dependence of $\Delta R/R_P$ on σ_{NM}/σ_{FM} while the $\beta = 0.8$ (blue), 0.6 (red), 0.4 (black), the $x = 1000$ nm, and the $\lambda_{FM} = 10$ nm. For getting a non-zero magnetoresistance, σ_{NM} must be at least 100 times larger than σ_{FM} , although normally the σ_{NM} is smaller than σ_{FM} or nearly equal to σ_{FM} in semiconductors. In the conductivity mismatch situation, the spin injection efficiency becomes extremely low. It seems that the injected spin absorbed by the ferromagnet as spin injector and then the spin is flipped fast inside ferromagnet. Obviously, the spin injection into semiconductor counters the obstacle with this conductivity mismatch problem.

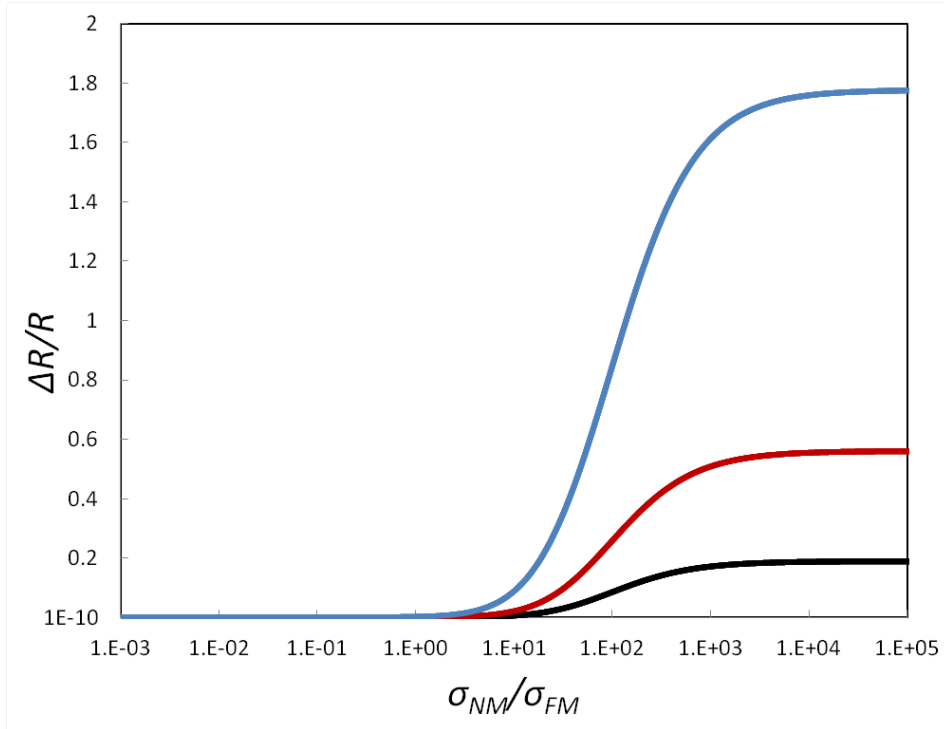


Figure 2.1.1 Dependence of $\Delta R/R_P$ on σ_{NM}/σ_{FM} while the $\beta = 0.8$ (blue), 0.6 (red), 0.4 (black), the $x=1000$ nm, and the $\lambda_{FM} = 10$ nm

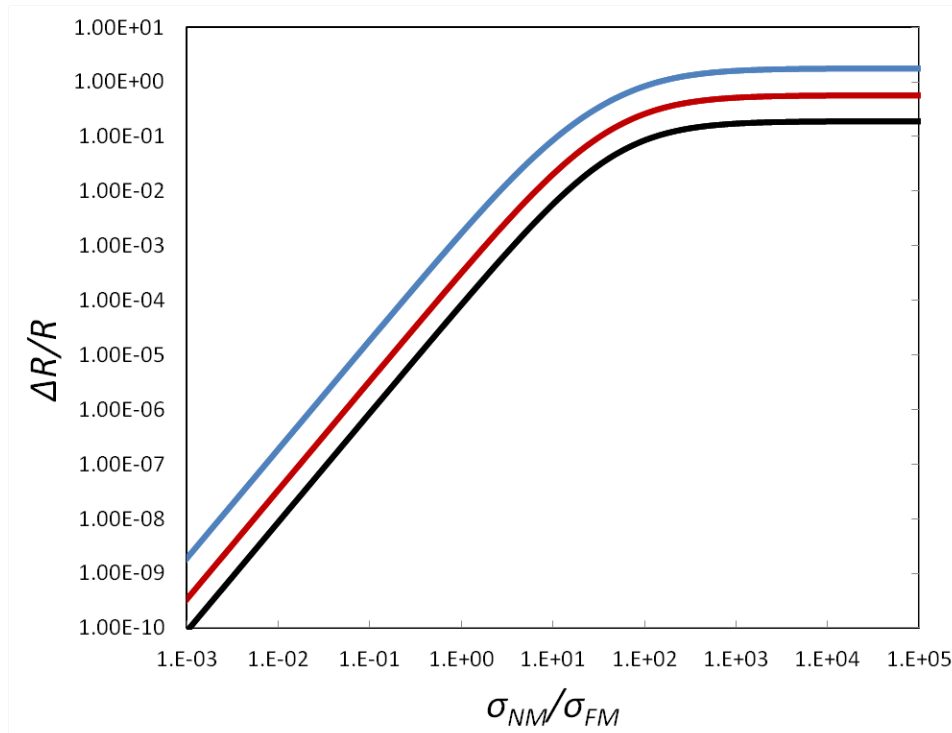


Figure 2.1.2 Logarithm scale for dependence of $\Delta R/R_P$ on σ_{NM}/σ_{FM} while the $\beta = 0.8$ (blue), 0.6 (red), 0.4 (black) and the $\lambda_{FM} = 10$ nm.

For overcoming the obstacles, there are several solutions.

- (1) 100% polarized spin injector and detector
- (2) Ballistic transport at the ferromagnet and semiconductor interface
- (3) Schottky barrier between ferromagnet and semiconductor

The (1) and (2) are difficult for applying the semiconductor because it is unrealistic for getting a perfect ferromagnet crystal quality.

2.1.2 Spin injection thorough interfacial tunneling barrier

The previous Schmidt model can not be applied for a realistic situation. Because, the ferromagnet/non-ferromagnet interface generally have a certain initial interface resistance even if metal/metal interface. The interface resistance virtually must play roll for the boundary condition. Anyway, elimination of the chemical potential continuity is important technique for spin injection efficiency enhancement. In this section, thus, the interfacial tunneling barrier is focused on. It is one of the most promising solutions for efficient spin injection from ferromagnet. Fert et al extended the theoretical calculation of the conductivity mismatch by developing a model in which as, spin dependent interface resistance is taken into account. [3] First, the spin dependent current density from ferromagnet to semiconductor is defined $J_{\pm}(z)$. The spin dependent conductivity is written to $\rho_{\uparrow\downarrow} = 2(1 - \beta)\rho_F^*$ and $\rho_{\uparrow\downarrow} = 2\rho_N^*$ for ferromagnet and non-ferromagnet, respectively. As considered to chemical potential discontinuity by interface resistance, the specific boundary condition in ferromagnet/non-ferromagnet interface ($z=z_0$) is described to

$$\mu_{\pm}(z = z_0^+) - \mu_{\pm}(z = z_0^-) = r_{\pm}J_{\pm}(z)(z = z_0) \quad (2.3.8)$$

where $\mu_{\pm}(z = z_0^+)$, $\mu_{\pm}(z = z_0^-)$ are the chemical potential in the two ferromagnet/non-ferromagnet interface, and interface resistance factor is expressed by interface resistivity r_b^*

$$r_{\pm} = 2r_b^*(1 \mp \gamma) \quad (2.1.9)$$

The spin resistance for ferromagnet r_F and non-ferromagnet r_N is defined to

$$\begin{aligned} r_F &= \rho_F^* \times l_{sd}^F \\ r_N &= \rho_N^* \times l_{sd}^N \end{aligned} \quad (2.1.10)$$

The r_b^* in the ferromagnet/non-ferromagnetic metal generally show around $10^{-3} \Omega\mu\text{m}^2$, which initially $r_F \ll r_N$ can be hold. In spin valve configuration, spin current polarization $SP = (J_+ - J_-)/J$ is written to

$$SP = \frac{\beta r_F + \gamma r_b^*}{r_F + r_N + r_b^*} \quad (2.1.11)$$

In case of conductivity mismatch dominated $r_b^* \sim 0$, the equation transform to

$$SP = \frac{\beta}{1 + r_N/r_F} \quad (2.1.12)$$

which is same equation of Schmidt model as discussed before. On the other hand, when r_b^* is much larger than r_F and r_N , the equation become to $SP = \gamma$. It is explained by the differences of spin diffusion length between ferromagnet and semiconductor. In condition of $r_b^* \sim 0$, the chemical potential at the interface become continuity. It causes the spin current relaxation inside ferromagnet near the interface. The spin diffusion length of ferromagnet is much shorter than that of non-ferromagnet, the almost all the spin flips in reaching the interface. In contrast, in situation of $r_b^* \gg r_F$, the spin diffusion length of the ferromagnet does not affect any interface spin relaxation, because the chemical potential hold discontinuity. At these results, the interface resistance makes it possible to suppress the conductivity mismatch problem. The magnetoresistance in ferromagnet/non-ferromagnet/ferromagnet structure is expressed with these ferromagnets boundary condition to:

$$\Delta R = \frac{2(\beta r_F + \gamma r_b^*)^2}{r_F + r_b^* \cosh\left(\frac{x}{l_{sd}^N}\right) + \frac{r_N}{2} \left[1 + \left(\frac{r_b^*}{r_N}\right)^2\right] \sinh\left(\frac{x}{l_{sd}^N}\right)} \quad (2.1.13)$$

$$\begin{aligned}
R_p &= 2(1 - \beta^2)r_F + r_N \frac{x}{l_{sd}^N} + 2(1 - \gamma^2)r_b^* \\
&+ 2 \frac{(\beta - \gamma)^2 r_F r_b^* + r_N (\beta^2 r_F + \gamma^2 r_b^*) \tanh\left(\frac{x}{2l_{sd}^N}\right)}{(r_F + r_b^*) + r_N \tanh\left(\frac{x}{2l_{sd}^N}\right)}
\end{aligned} \tag{2.1.14}$$

where x is the non-ferromagnet length (spin travel length). As considered to three specific conditions, the magnetoresistance is described as listed below.

(1) Without interface resistance $r_b^* \sim 0, r_N \sim r_F,$

$$\frac{\Delta R}{R} = \frac{\beta^2}{(\beta - 1)(\beta + 1)} \tag{2.1.15}$$

(2) Without interface resistance + semiconductor regime $r_b^* \sim 0, r_N \gg r_F$

$$\frac{\Delta R}{R} = 2\beta^2 \left(\frac{r_F l_{sd}^N}{r_N x} \right)^2 \tag{2.1.16}$$

(3) With interface resistance + semiconductor regime $r_b^* \neq 0, r_N \gg r_F$

(i) $r_N \left(\frac{x}{l_{sd}^N} \right) < r_b^* < r_N \left(\frac{l_{sd}^N}{x} \right),$

$$\Delta R = 2\gamma^2 r_b^*, \quad \frac{\Delta R}{R} = \frac{\gamma^2}{1 - \gamma^2} \tag{2.1.17}$$

(ii) $r_N \left(\frac{l_{sd}^N}{x} \right) < r_b^*,$

$$\frac{\Delta R}{R} = \frac{2r_N l_{sd}^N}{(1 - \gamma^2)r_b^* x} \tag{2.1.18}$$

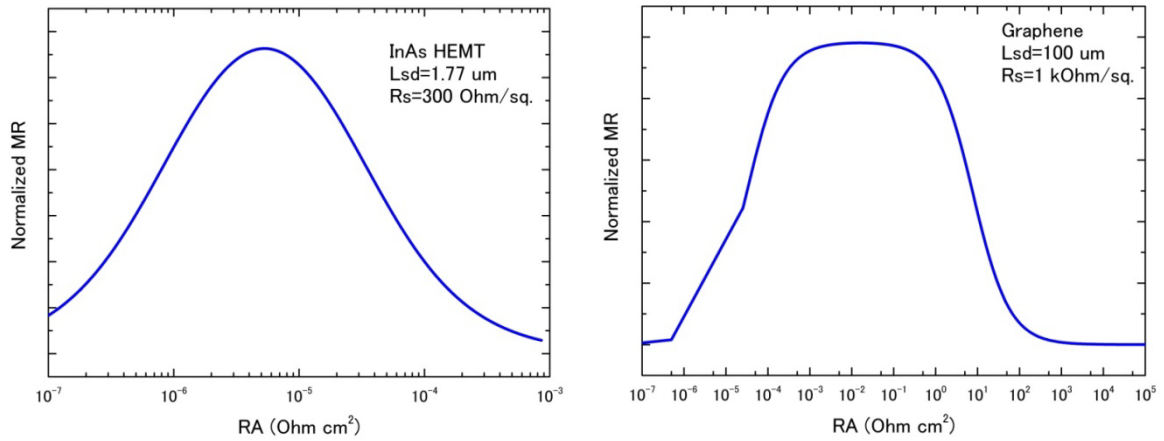


Figure 2.1.3 The magnetoresistance versus contact resistivity in InAs QW and Graphene

Figure 2.1.3 shows the magnetoresistance dependent on contact resistivity for InAs QW and graphene as comparison. In the conductivity mismatch region, the $\Delta R/R$ increase constantly as proportional to ΔR enhancement, and then it reaches maximum at $r_b^* = r_N$ point. While, $\Delta R/R$ gradually decreased in increasing the r_b^* for increase of only the R . To evaluate material parameter, non-doped non-ferromagnets are compared here. Since the InAs QW has a relatively high conductivity and a short spin diffusion length compared to graphene, the spin resistivity is lower. This means that ideal interface resistance for efficient spin injection become lower. It is obviously emphasized that alignment between interface resistance and spin resistance is crucial to detect non-zero magnetoresistance according to material parameters.

2.2 Spin transport in semiconductor

The amount of injected spin into semiconductor doesn't directly response to magnetoresistance. The deterioration of magnetoresistance can be occurred due to unintentional spin relaxation and precession inside semiconductor channel. The dynamics of magnetoresistance deterioration is related to each semiconductor material and device structures. Thus, it is important to understand the spin relaxation and precession mechanism for precise device control and design.

2.2.1 Spin relaxation

Spin relaxation is the depolarization (randomization) of spin density inside non-ferromagnet material for reaching to initial non-equilibrium state, which means that conducted spin flips and never come back to polarized state. It is occurred due to combination of momentum scattering and spin orbit interaction. The relaxation rate is defined as a certain time (τ_S) and length (λ_S), as called spin life time and spin relaxation length respectively. The relation of spin life time and relaxation length can be described by using diffusion constant D , which gives

$$D = \lambda_S / \tau_S^2 \quad (2.2.1)$$

According to the Einstein's relation, the diffusion constant D is written to

$$D = \frac{\sigma}{e^2 \rho_{DOS}(E)}. \quad (2.2.2)$$

where σ is the Drude conductivity and $\rho_{DOS}(E)$ is the density of state. Here, electron is conducted by drift but electrons within kT around the Fermi energy $kT \ll E_F$. It means that the first level in two dimensional electron systems is dominant, Fermi wave number k_F and Fermi energy E_F

$$k_F = \sqrt{2\pi n_S} \quad (2.2.3)$$

$$E_F = \frac{\hbar^2 k_F^2}{2m^*} = \frac{\pi \hbar^2}{m^*} \quad (2.2.4)$$

where n_S is the carrier density. Whereby, density of state at Fermi energy in two dimensional electron systems is expressed as

$$\rho_{2D}(E_F) = \frac{m^*}{\pi \hbar^2} \quad (2.2.5)$$

The diffusion constant D can also be written as,

$$D = \frac{1}{e^2 \rho_{2D}(E_F) R_S}. \quad (2.2.6)$$

where R_S is the sheet resistance.

The spin life time and spin diffusion length is regarded as a particular index which each semiconductors have. These parameters indicate that individual semiconductor materials have spin-related transport characteristics. The spin life time (diffusion length)

have range from several hundred pico-seconds to nan-seconds (from nano-meter to micro-meter), although it depends on material properties such like doping concentration, carrier mobility, band structures and so on. It has been cleared that several factors cause to spin relaxation and de-phasing. Here, the physical origin of each relaxation mechanism is listed up in the following.

Elliot-Yafet (EY) mechanism

EY mechanism [4-5] refer to the conducted spin relaxation in which an electron spin scatter through impurities and phonon scattering event that induce to flip the spin. These momentum scattering event can be originated from impurity doping and defect, lattice vibration (thermal effect), and ionized impurity. The spin flip-flop mechanisms are illustrated in Fig. 2.4. The localized electric field due to these factors is directly transformed to spin orbit interaction. Almost all semiconductors have the EY mechanism, particularly this mechanism is much concerned in highly doped semiconductors and inversion symmetric material of group **IV**, such like Si and Ge. The spin life time for EY mechanism is given by the relation:

$$\frac{1}{\tau_s(E_k)} = A \left(\frac{\Delta_{SO}}{E_g + \Delta_{SO}} \right)^2 \left(\frac{E_k}{E_g} \right)^2 \frac{1}{\tau_{ms}(E_k)} \quad (2.2.7)$$

Where A is a constant (almost near to 1), Δ_{SO} is the spin-split energy in the valence band, E_g is the bandgap, and τ_{ms} is the momentum scattering time. Since the momentum scattering event is typically dominant of lattice phonons scattering around room temperature and impurities at low temperature,

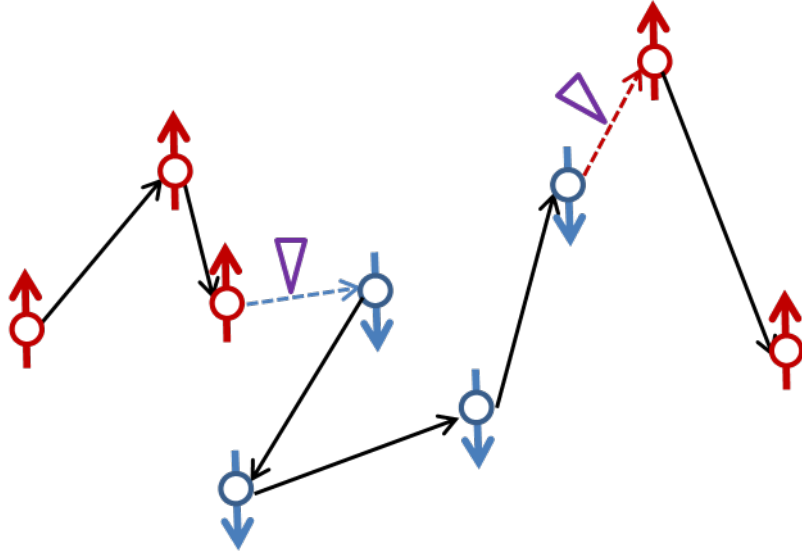


Figure 2.2.1 Illustration of the Elliot-Yafet spin relaxation mechanism.

D'yakonov-Perel' (DP) mechanism

DP mechanism [6] is originated from the spin-split of the conduction band related to spin orbit interaction of structural inversion asymmetry (SIA) and bulk inversion asymmetry (BIA) (see section 2.4.2 and 2.4.3). The conducted spin move precession by a certain precession frequency with respect to lattice orientation $\vec{\Omega}(\vec{k})$ in effective magnetic fields via SIA and BIA. The wave number k is shifted through the momentum scattering events, and then the orientation of effective magnetic field can be also changed. During the time between scattering event, the spin precession phase is shifted by $\vec{\Omega}(\vec{k}) \tau_{ms}$, where τ_{ms} is the momentum scattering time. Hence, spin life time related to DP spin relaxation is expressed to

$$\frac{1}{\tau_s} \approx \Omega^2 \tau_{ms} \quad (2.2.8)$$

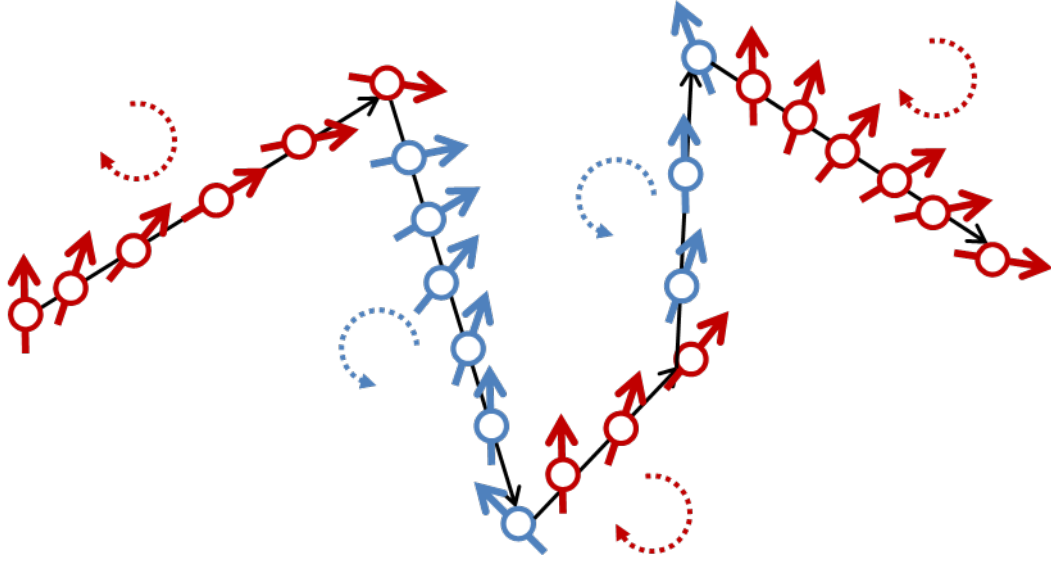


Figure 2.2.2 Illustration of the D'yakonov-Perel' mechanism. The conducted spin precesses aligned to effective magnetic field by spin orbit interaction.

The two major spin scattering mechanism is important to understand. The scattering rate of EY mechanism is linearly proportional to momentum scattering time $\tau_S^{EY} \propto \tau_{ms}$, while that of DP mechanism is inversely proportional to it $\tau_S^{DP} \propto \frac{1}{\tau_{ms}}$. It implies that low momentum scattering time τ_{ms} make the τ_S^{DP} possibly enhanced, which spin precession frequency become much higher by using in engineering quantum confinement, because it is well known that the quantum confinement normally increase the momentum scattering time. To be concluded, a high mobility and quantum confinement structure have much advantage for application of spin-FET.

2.2.2 Structural Inversion asymmetry (SIA)

Spin orbit coupling is expressed by Dirac equation from Hamiltonian;

$$H = \frac{\hbar}{2m^2c^2} \vec{\sigma} \cdot (\vec{p} \times \nabla V) \quad (2.2.9)$$

where \vec{p} is the momentum, $\vec{\sigma}$ is the spin operators and V is the electrostatic chemical potential. The effective spin orbit interaction is drastically increased in conduction band

of semiconductor which can be written via $k \cdot p$ perturbation;

$$H = \frac{P^2}{3} \left[\frac{1}{E_0^2} - \frac{1}{(E_0 + \Delta_0)^2} \right] \frac{1}{\hbar} \vec{\sigma} \cdot (\vec{p} \times \nabla V) \quad (2.2.10)$$

Structural inversion asymmetry refers to the conducted electron feel effective magnetic field in asymmetric confinement potential of conduction band, as shown in Fig. 2.5. The asymmetry electrical potential supply conducted to an effective magnetic by a certain precession frequency which is given by:

$$\vec{\Omega}(\vec{k}) = \alpha_R \vec{\sigma} \times \vec{k} \quad (2.2.11)$$

where α_R is the strength of the spin orbit coupling (Rashba parameter). [7] This effective magnetic field make the conduction s-orbit band degenerated, which leads that spin polarization is occurred in biased voltage gradient. The one dimensional energy dispersion along to z-direction in a semiconductor quantum well form split as described to

$$E_k^{\uparrow\downarrow} = \frac{\hbar^2}{2m^*} ((k_x \pm k_R)^2 - k_R^2) \quad (2.2.12)$$

where m^* is the effective mass in the conduction band and $k_R = \alpha_R m / \hbar^2$. Hamiltonian is also expressed to:

$$H_R = \frac{\alpha_R}{\hbar} \vec{\sigma} \cdot (\vec{p} \times \hat{z}) = \frac{\alpha_R}{\hbar} (p_y \sigma_x - p_x \sigma_y) \quad (2.2.13)$$

Whereby, the spin split energy linearly depends on strength of spin orbit coupling and Fermi wave number as given to:

$$\Delta_R = 2\alpha_R k_F \quad (2.2.14)$$

The spin split energy reach to more than 30 meV in InAs quantum well in highly engineered structure.

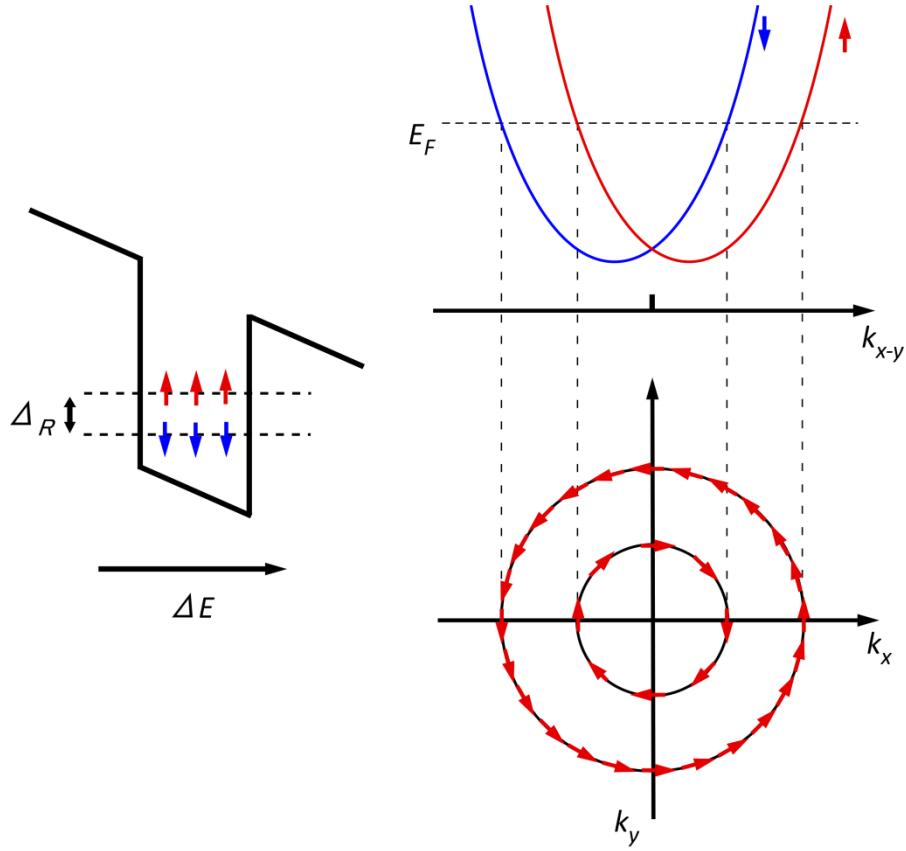


Figure 2.2.3 Illustration of the degenerated spin split band in narrow gap quantum well, the energy dispersion relation to k -space, and effective magnetic field in field of SIA.

2.2.3 Bulk inversion asymmetry (BIA)

Bulk inversion asymmetry comes from lattice structure asymmetry as represented to zinc-blend structure of III-V type compound semiconductors (GaAs, InAs, InP). [8] In the zinc-blend lattice structure, the atoms position breaks inversion asymmetry, that is electric field due to Coulomb potential between III-V atoms. The spin orbit interaction emerge in which the spin conduct in the electric field. The Hamiltonian is written as precession frequency:

$$H = \frac{\hbar}{2} \vec{\sigma} \cdot \vec{\Omega}(\vec{k}) \quad (2.2.15)$$

The precession frequency is derived from $k \cdot p$ perturbation of zinc-blende structure which is given by:

$$\begin{aligned}
H &= \frac{\hbar}{2} \vec{\sigma} \cdot \vec{\Omega}(\vec{k}) \\
&= \frac{\alpha_D \hbar^2}{(2m^* E_g)^2} \left(k_x(k_y^2 - k_z^2), k_y(k_z^2 - k_x^2), k_z(k_x^2 - k_y^2) \right)
\end{aligned} \tag{2.2.16}$$

where α_D is the strength of the spin orbit interaction (Dresselhaus parameter), and E_g is the energy band gap of the semiconductor. Compared to the SIA, the BIA have anisotropic field to the k -space. It assumes that the two dimensional electron gas on (001) crystallographic orientation in the following form:

$$H = \frac{\alpha_D}{\hbar} (k_y \sigma_y - k_x \sigma_x) \tag{2.2.17}$$

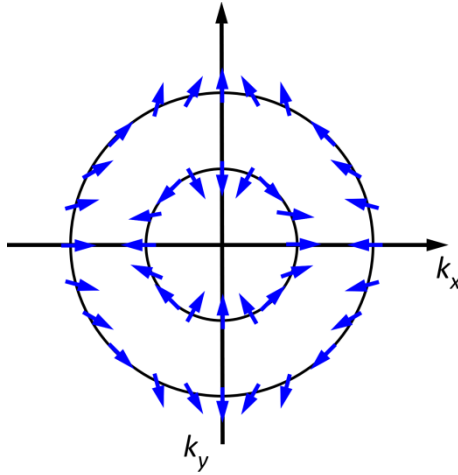


Figure 2.2.4 Illustration of the effective magnetic field due to linear BIA effect.

2.3 Spin injection and detection measurement

Spin injection and detection measurement in spin valve geometry is discussed here. Spin valve signal must be taken careful to analyze because another effect usual include it. The magnetoresistance is a simply resistance change as ferromagnets orientation by magnetic field. In this situation, the anomalous Hall effect and anisotropic magnetoresistance (AMR) effect, as no related to spin injection, appear at the same time.[12] In this reason, non-local measurement have been developed to eliminate these unambiguous signals in spin valve measurement.

2.3.1 Two-terminal local geometry

The two-terminal local spin valve measurement is simply analogous to the inserted non-ferromagnet in metallic GMR or TMR device, where Spin polarized electron injected to non-ferromagnet by biased electric field between two ferromagnet which imposed on non-ferromagnet, the magnetoresistance appear depending on parallel and anti-parallel state of two ferromagnets magnetization.

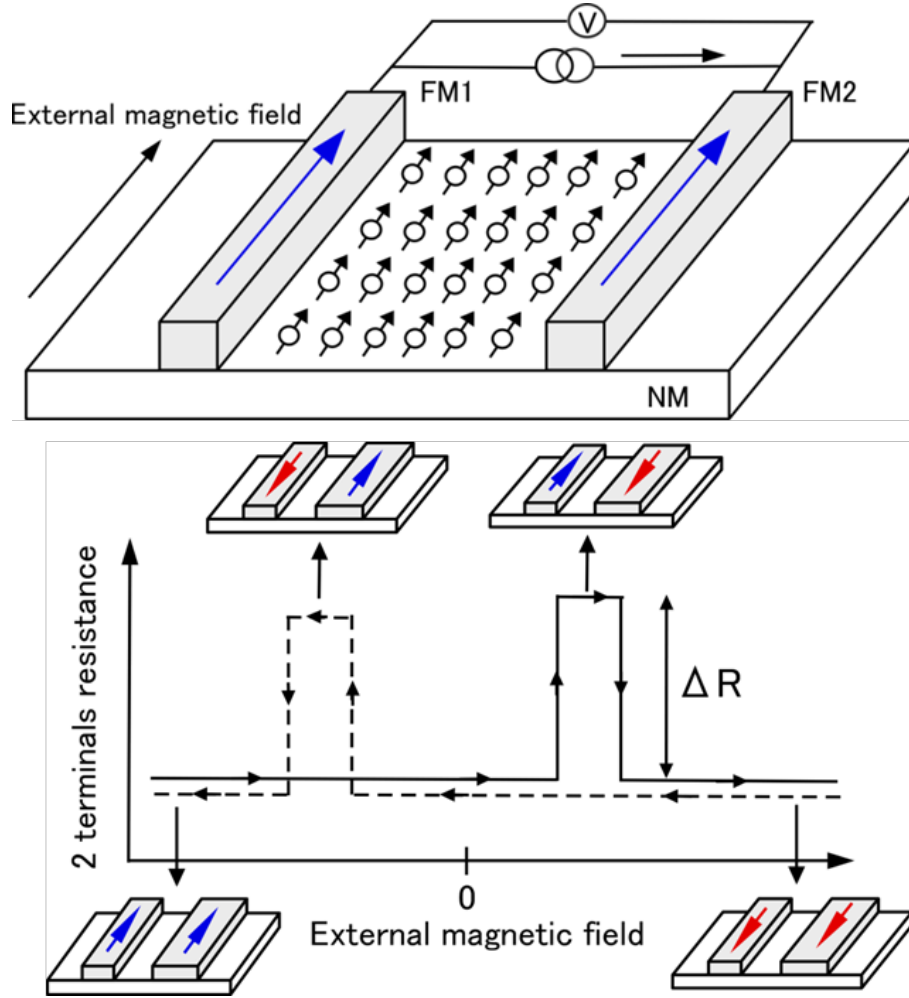


Figure 2.3.1 Schematics of the two terminal local spin valve configuration and ideal spin valve signals

As described in section 2.1, the amplitude of magnetoresistance is expressed below.

$$\Delta R = \frac{2(\beta r_F + \gamma r_b^*)^2}{r_F + r_b^* \cosh\left(\frac{x}{l_{sd}^N}\right) + \frac{r_N}{2} \left[1 + \left(\frac{r_b^*}{r_N}\right)^2\right] \sinh\left(\frac{x}{l_{sd}^N}\right)} \quad (2.3.1)$$

$$\begin{aligned}
R_p &= 2(1 - \beta^2)r_F + r_N \frac{x}{l_{sd}} + 2(1 - \gamma^2)r_b^* \\
&+ 2 \frac{(\beta - \gamma)^2 r_F r_b^* + r_N (\beta^2 r_F + \gamma^2 r_b^*) \tanh\left(\frac{x}{2l_{sd}}\right)}{(r_F + r_b^*) + r_N \tanh\left(\frac{x}{2l_{sd}}\right)}
\end{aligned} \tag{2.3.2}$$

2.3.2 Four-terminal nonlocal geometry

The four-terminal non-local spin valve configuration makes it possible to detect only spin injection and detection related phenomena as shown in Fig. 2.4.1. The biased current in injector supply a pure spin current between injector and detector, while spin and charge current between outside electrode and injector. The pure spin current diffusive to the detector orientation, and then it is detected by ferromagnet detector. It means that there are no charge current in the detector circuit resulted to elimination of local Hall effect and anisotropic magnetoresistance.

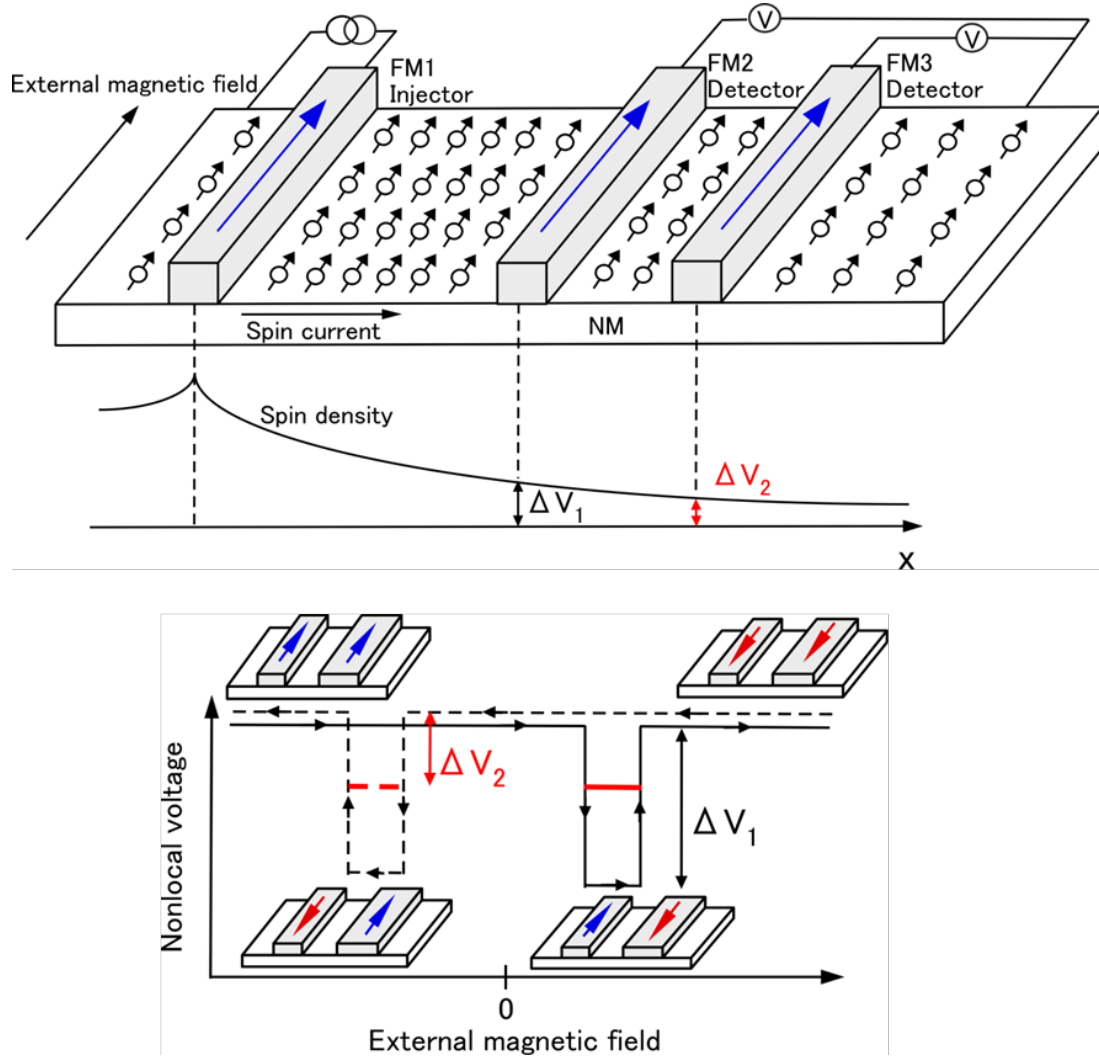


Figure 2.3.2 Schematics of the four-terminal non-local spin valve configuration and ideal spin valve signals.

The spin transfer characteristic in the nonlocal set-ups was developed theoretically by S. Takahashi and S. Maekawa. [13] For easier to understand, it assumes that spin current at the ferromagnet and non-ferromagnet interface is uniform as according to $l_{sd}^F \ll d_N, d_F \ll w_N, w_F \ll l_{sd}^N$, where $d_{N(F)}$ and $w_{N(F)}$ are non-ferromagnet (ferromagnet) width and thickness. The current in the interface is described by $I = 1/(eR_i)$. In this situation, when the bias current I flow between ferromagnet injector (FM1) and outside non ferromagnet, there are no charge current between FM and FM2. The electrical chemical potential dependent on x direction is written to $\mu_-(x) = eIx/\sigma + \sigma\delta\mu$ between FM1 and NM and $\mu_+(x) = \sigma\delta\mu$ for between FM1 and FM2, where $\delta\mu$ is the

$\delta\mu = \alpha_1 \exp\left(-\frac{|x|}{l_{sd}^N}\right) + \alpha_2 \exp\left(-\frac{|x-L|}{l_{sd}^N}\right)$ with chemical potential shift by spin

injection term α and FM2 detector (x-L).

The nonlocal spin signals in FM2 correspond to the spin chemical potential difference at the FM2 interface in three cases, is given by

$$\Delta R_{NL} = \frac{4R_{SC} \left[\frac{P_I}{1-P_I^2} \left(\frac{R_I}{R_{SC}} \right) + \frac{P_{FM}}{1-P_{FM}^2} \left(\frac{R_{FM}}{R_{SC}} \right) \right]^2 \exp\left(-\frac{L}{\lambda_{SC}}\right)}{\left[\frac{2}{1-P_I^2} \left(\frac{R_I}{R_{SC}} \right) + \frac{2}{1-P_{FM}^2} \left(\frac{R_{FM}}{R_{SC}} \right) + 1 \right]^2 - \exp\left(-\frac{2L}{\lambda_{SC}}\right)} \quad (2.3.3)$$

where the $R_{SC(F)} = \rho_{SC(F)} \lambda_{SC(F)} / (d_{N(F)} w_{N(F)})$.

2.3.3 Hanle effect

The Hanle effect relates to spin precession effect in external magnetic field. It assumes that conducted spin diffusive only in a 1-D-diffusive channel between two ferromagnets. The perpendicular external magnetic field make the conducted spin torque, resulted to induce spin precession. The diffusion time t from injector to detector has a broad distribution $\varphi(t)$, which is expressed by

$$\varphi(t) = \frac{1}{\sqrt{4\pi Dt}} \exp\left(\frac{-L^2}{4Dt}\right) \quad (2.3.4)$$

During the spin travel between ferromagnet, spin coherence also diffusive leading to spin population decay. It causes that only non-flip-flop spin is detectable in Hanle geometry. In this reason, taking into account the spin flip process, the output signal become multiple the $\varphi(t)$ and spin flip process function. Then, probability of spin potential diffusion is expressed to $\varphi(t) \exp(-t/\tau_{sd})$. Since the detectable spin also depends on the spin precession angle $\cos(\omega_L t)$ in center of z-direction at the detector. Finally, the output signal is written with integration of all diffusion time by

$$V_{NL}(B_{\perp}) = \frac{IP^2}{eN(E_F)S} \int_0^{\infty} \varphi(t) \cos(\omega_L t) \exp\left(\frac{-t}{\tau_{sd}}\right) dt \quad (2.3.5)$$

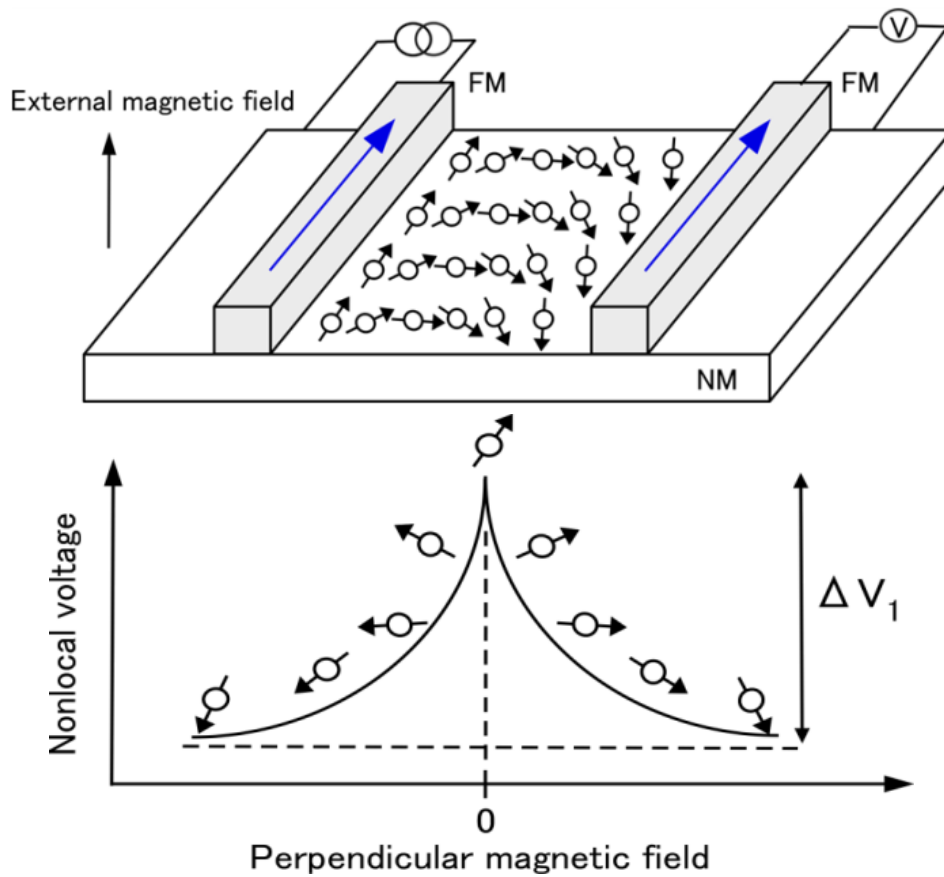


Figure 2.3.3 Schematics of Hnle effect measurement

2.4 Spin FET

Spin FET is based on the combination of spin injection and detection and spin manipulation by spin orbit interaction in a strictly ballistic 1-D system. Taking into account the strong SIA materials (e.g. InAs QW), the conducted spin precession depends on the initial spin angle. Figure 2.4.1 shows the initial spin angle (magnetization direction) dependent on spin precession. When y-magnetized spin is injected to InAs QW, the spin precession does not occur, because the SIA direction and spin quantization axis stay parallel state. On the other hand, when x and z-magnetized spin is injected, the SIA is anti-parallel to injected spin resulted to spin precession in center of y-axis. The two precession geometries are only different with spin precession phase caused by 90 degree of the initial phase shift. The spin precession angle is expressed to:

$$\Delta\theta = \frac{2\alpha(V_g)m^*L}{\hbar^2} \quad (2.4.1)$$

where the $\alpha(V_g)$ is the SOI strength dependant on gate voltage. The observable conductance modulation ΔG is also written to:

$$\Delta G = A \cos\left(\frac{2\alpha(V_g)m^*L}{\hbar^2} + \phi\right) \quad (2.4.2)$$

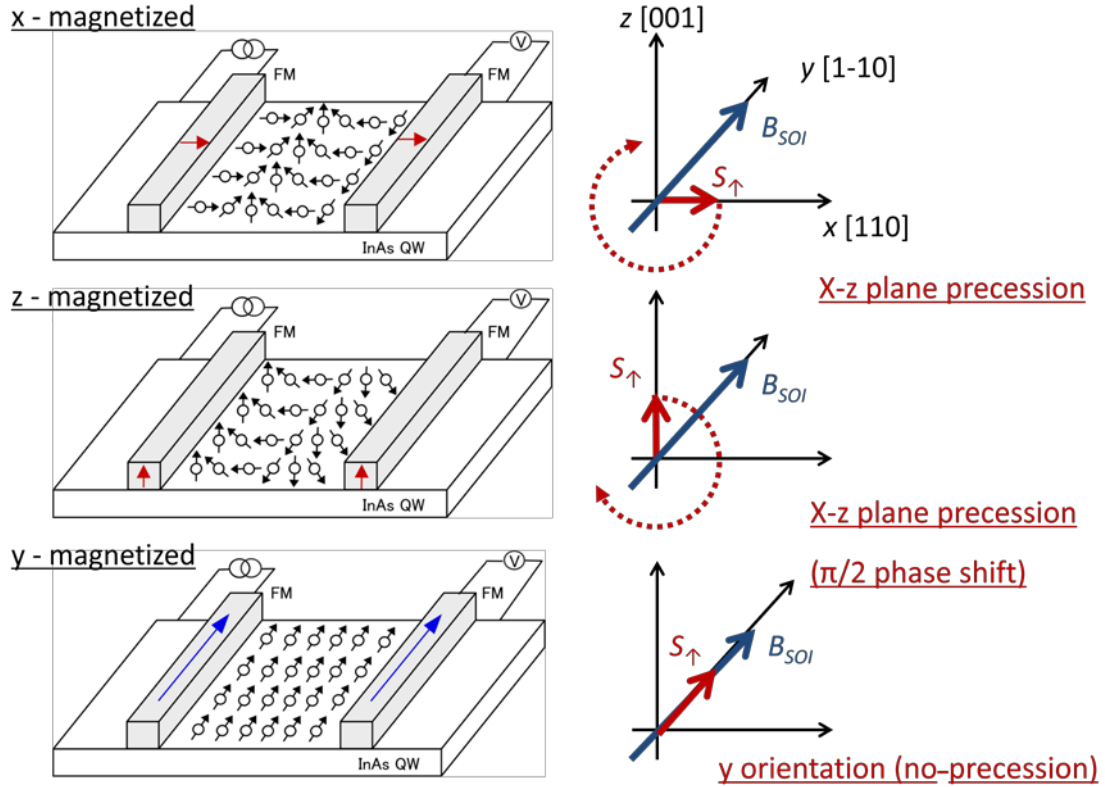


Figure 2.4.1 Spin precession and non-precession configuration in 1-D InAs QW.

2.4.1 Spin FET in two dimensional system

In two dimensional quasi-ballistic regimes, the wave number for channel width (y) direction was not conserved. Since the total wave number is expressed to $(k_F^2 - k_y^2)^{-1/2}$, the momentum scattering event in y-direction can make spin randomized. Taking into account the total wave number $(k_F^2 - k_y^2)^{-1/2}$, the conductance modulation in a two dimensional spin FET is written with precession angle $\theta(k_F, k_y, \alpha(V_g))$ to [15]:

$$\Delta G = \frac{q^2 W}{2\pi h} \int_0^{k_F} \left(1 - \frac{k_y^2}{k_F^2}\right) \cos \left[\theta(k_F, k_y, \alpha(V_g)) L \right] \quad (2.4.3)$$

$$\theta(k_F, k_y, \alpha(V_g)) = - \frac{\frac{2m^* \alpha(V_g)}{\hbar^2} + \frac{4m^{*2} \alpha^2(V_g)}{\hbar^4}}{\sqrt{k_F^2 - k_y^2}} \quad (2.4.4)$$

$$\Delta G \approx \frac{\hbar B}{2\sqrt{\pi m^* \alpha(V_g) L}} \cos \left[\frac{2m^* \alpha(V_g) L}{\hbar^2} + \frac{\pi}{4} \right] \quad (2.4.5)$$

Thus, the conductance modulation ratio in 2-D spin FET is limited to be less than 100 % caused by the existence of y-direction momentum scattering event as compared eq. (2.4.2) and (2.4.5). It implies that on/off ratio of 2-D spin-FET stay to be weak, even if extremely high spin accumulation is realized. Only option for overcoming this problem is the strictly 1-D channel, although on-resistance of the 1-D spin FET limited more than quantum resistance h/e^2 (>10 kOhm). It is impossible for the spin FET to attain high driving current and on/off ratio simultaneously, unlike conventional MOSFET.

Bibliography

- [1] M. Johnson and R. H. Silsbee, Phys. Rev. Lett. 55, 1790 (1985).
- [2] G. Schmidt, Phys. Rev. B 62, 8 (2000).
- [3] A. Fert and H. Jaffr es, Phys. Rev. B 64, 184420 (2001).
- [4] R. J. Elliott, Phys. Rev. 96, 266 (1954).
- [5] Y. Yafet, Physics Letters A 98, 287 (1983).
- [6] M. Dyakonov, and V. Perel, Soviet Physics Solid State, USSR 13, 3023 (1972).
- [7] E. I. Rashba, Phys. Rev. B 62, 162671 (2000).
- [8] G. Dresselhaus, Phys. Rev. 100, 580 (1955).
- [9] R.W. Wood and A. Ellett, Phys. Rev. 24, 243 (1924).
- [10] W. Hanle, Z. Phys. 30, 93 (1924).
- [11] M. Dyakonov, “*Spin physics in semiconductors*” (2008) Springer Press
- [12] F. G. Monzon and M. L. Roukes, J. Mag. Mag. Mat. 198, 632 (1999).
- [13] S. Takahashi and S. Maekawa, Phys. Rev. B 67, 052409 (2003).
- [14] H. C. Koo, J. H. Kwon, J. Eom, J. Chang, S. H. Han and M. Johnson, Science 325, 1515 (2009).
- [15] P. Agnihotri and S. Bandyopadhyay, Physica E 42, 1736 (2010).

Chapter 3

Experimental Methods

3.1 Sample fabrication

In this short section, the fabrication process for analyzed samples is described as details. First one is a gated Hall-bar fabricated for Hall measurement. The main objective is the gated process in InAs quantum well. Last one is a lateral spin valves for Si and InAs QW.

3.1.1 Gated Hall bar

The fabrication process of this device is done by conventional optical lithography, wet chemical etching, plasma enhanced chemical vapor deposition and metal evaporator. In forming a Pd/InAlAs Schottky gate, leakage current make a trouble in mesa side wall. For decreasing the leakage curret, InAs/InGaAs composite channel was etched by citric acid based etchant without InAlAs layer etched. The following is the flow for device fabrication.

(1) Mesa isolation formation

Prebake	90 degree for 10 min
Spin coat	SPR6810, 500/5000 rpm, 3/30 s
Bake	90 degree for 10 min
Exposure	
Development and Rinse	

Wet chemical etching $\text{H}_3\text{PO}_4:\text{H}_2\text{O}_2:\text{H}_2\text{O}$ 30:1:1, 15 degree, 100s

(220 nm of mesa height)

Selective etching for InAs/InGaAs from mesa side wall

$\text{C}_6\text{H}_7\text{O}_8:\text{H}_2\text{O}_2:\text{H}_2\text{O}$ 2:1:2 for 4min

Resist removal

(2) Passivation film

Native oxide removal $\text{NH}_3:\text{H}_2\text{O}$ 1:3 for 30 sec

SiO_2 deposition PE-CVD (250 nm)

(3) Ohmic electrode formation

Photolithography for Ohmic electrode pattern

SiO_2 etching $\text{HF}:\text{NH}_4\text{F}$ 1:5 for 30 sec

Native oxide removal $\text{NH}_3:\text{H}_2\text{O}$ 1:3 for 30 sec

Metal deposition Au/Ge/Au/Pd/Au 30/40/30/15/50 nm

Rapid thermal Annealing 420 degree for 75 sec

Lift off

(4) Gate formation

Photolithography for SiO_2 etching pattern

SiO_2 etching $\text{HF}:\text{NH}_4\text{F}$ 1:5 for 30 sec

Photolithography for Gate pattern

Native oxide removal $\text{NH}_3:\text{H}_2\text{O}$ 1:3 for 30 sec

Metal deposition Pd(30)/Ti(20)/Au(50) nm

Lift off

3.1.2 Lateral Spin Valve

The lateral spin valve for n-Si and InAs QW was fabricated by electron beam lithography, reactive ion and wet chemical etching. The following is the flow for device fabrication for InAs QW as represented.

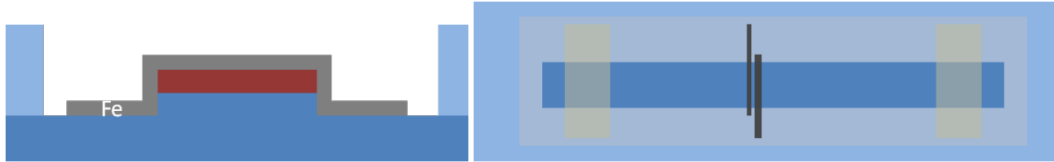
(1) Mesa isolation formation

Photolithography for isolation pattern

Wet chemical etching $\text{H}_3\text{PO}_4:\text{H}_2\text{O}_2:\text{H}_2\text{O}$ 30:1:1, 15 degree, 70s

Ferromagnet deposition

Lift off



(6) Supply Pad formation

Photolithography for Pad pattern

Metal deposition Ti/Au, 20/60 nm

Lift off

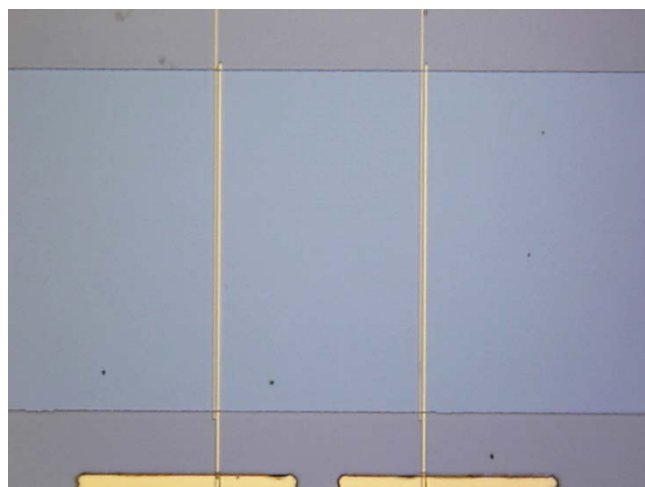
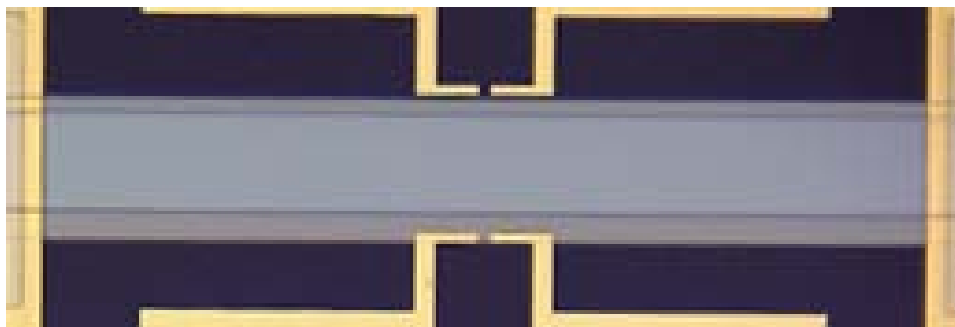
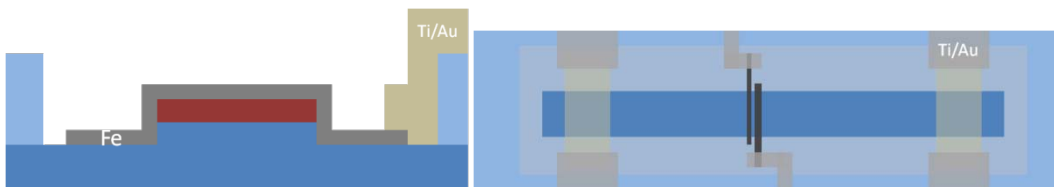


Figure 3.1 A fabricated lateral spin valve device picture.

3.2 Electrical measurement in an InAs quantum well

The layer sequence of an InAs quantum well is detailed in section 5.1. Conventional Hall and Shubnikov de Haas oscillation measurements were used to evaluate the carrier density, mobility and spin split energy in the InAs quantum well.

3.2.1 Shubnikov de Haas oscillation

A perpendicular magnetic field to a conducted carrier induces a Lorentz force which is perpendicular to the current orientation as known the Hall effect. The Hall resistance in 2-D structure is given by $R_H = (nR_S)^{-1}$ with sheet resistance R_S . The electron mobility μ is expressed $\mu = R_H/\rho$ where ρ is the sheet resistivity. When the magnetic field is enough to high in a clean 2D structure, the Hall resistance is quantized resulted to get step behavior. The resistance steps are characterized by h/ne^2 , where n is an integer, as called the von Klitzing constant. The origin is formation of the Landau levels which is degenerated due to the cyclotron orbits of carriers quantization. The Landau levels is given by $E_n = (n + 1/2)\hbar\omega_c$, where the $\omega_c = |eB|/m$ is the cyclotron frequency. The typical Shubnikov-de Haas oscillation is shown in figure 3.2.1. The length between oscillations peaks depend on the carrier density $n = e(\delta 1/B)/(\pi\hbar)$. In strong Rashba SOI, the Landau level is degenerated by the spin split energy resulted to form two oscillation frequencies as shown in Fig. 3.2.2. The strength of the spin orbit interaction can be extracted from the period of the beating $\Delta 1/B$ according to:

$$\alpha = \frac{\hbar \left(\Delta \frac{1}{B} \right)}{2m^*k_F} \quad (3.2.1)$$

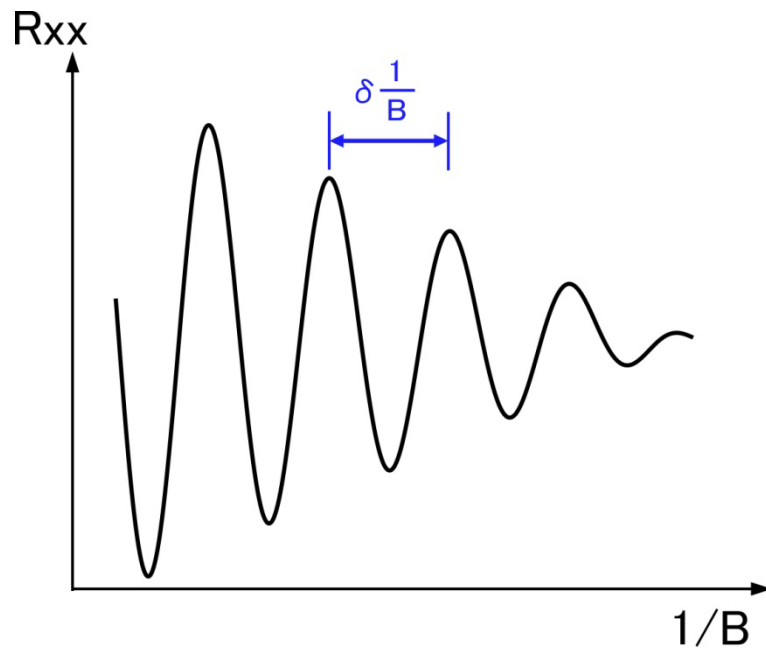


Figure 3.2.1 The Shubnikov-de Haas oscillation in weak spin orbit interaction

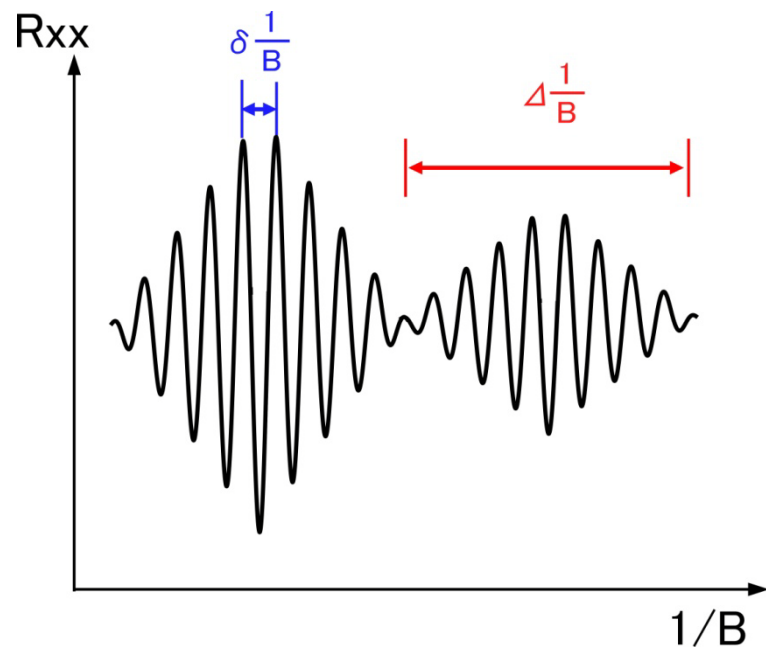


Figure 3.2.2 The Shubnikov-de Haas oscillation in strong spin orbit interaction

Chapter 4

Thermal stability of Pd Gate in Pseudomorphic InGaAs Heterostructures

-

4.1 Introduction

For high efficiency spin injection, a clean FM/InAs interface is crucial. However, Fe as ferromagnetic contact was shown to react with arsenide over thermal treatment of resist bake for electron-beam lithography caused to deteriorate spin injection efficiency. On the other hand, commonly used Schottky gate materials such as Ti/Au and Ti/Pt/Au on InAlAs barrier-layer are known to deteriorate during thermal procedure after the Schottky formation. For these reasons, I have investigated a heat-stable material for gate and forming gate contact before Fe contact formation to avoid this problem of heat treatments. Despite the fact that titanium is widely used as Schottky gate material on InAlAs, the Schottky characteristics have been shown to low Schottky barrier height and low heat stability. [1] Catalytic metals such as platinum or palladium have been known to a good Schottky material on GaAs or AlGaPb devices for precise Schottky barrier thickness control. [2-3] Recently, Pt/InAlAs Schottky control was reported. [4-5] Pt gate could be able to adjust the threshold voltage with appropriate anneal procedure causing to interface of alloy progressed (buried-Pt gate technology) and achieve high transconductance and large cut-off frequency. It was also reported that Pd and n-InAlAs

of Schottky diode can lead to good Schottky characterization as well. [6] Compared with platinum, palladium has advantages such as low cost and lower melting point which make easier to be evaporated by electron-beam evaporator. However, there have been only a few reports on Pd/InAlAs Schottky contact and almost no report on HEMT with Schottky material. In this section, we describe the fabrication and electrical evaluation of Hall-bar device on InGaAs-based pseudomorphic heterojunction with Pd gate in order to confirm the thermal stability of the material system.

4.2 InP HEMT structure

We used the $\text{In}_{0.53}\text{Ga}_{0.47}\text{As}/\text{In}_{0.52}\text{Al}_{0.48}\text{As}$ HEMT structure grown on InP(100) substrate with 50 Å -thick $\text{In}_{0.81}\text{Ga}_{0.19}\text{As}$ channel layer in the middle of the InGaAs layer. The device structures illustrated in Fig. 4.1. The structure consist of 300/800 nm of InP/ $\text{In}_{0.52}\text{Al}_{0.48}\text{As}$ buffer layer, $5.0 \times 10^{11} \text{ cm}^{-2}$ of Si δ -doping, 100 Å of $\text{In}_{0.52}\text{Al}_{0.48}\text{As}$ spacer layer, 50 Å of $\text{In}_{0.53}\text{Ga}_{0.47}\text{As}$ sub-channel, 50 Å of $\text{In}_{0.81}\text{Ga}_{0.19}\text{As}$ main channel, 50 Å of $\text{In}_{0.53}\text{Ga}_{0.47}\text{As}$ sub-channel, 100 Å of $\text{In}_{0.52}\text{Al}_{0.48}\text{As}$ spacer layer, $1.0 \times 10^{12} \text{ cm}^{-2}$ of Si δ -doping, 50 Å of $\text{In}_{0.52}\text{Al}_{0.48}\text{As}$ barrier layer and InGaAs 100 Å cap-layer. Gated hall-bar structure was fabricated for evaluation of annealing effect of Pd gate in a HEMT structure. The dimension of the Hall-bar devices were 50 μm wide and 150 μm long as shown in Fig. 4.1 and 4.2. The schematic conduction band diagram of the device before and after the anneal are shown in Fig. 4.3. In the figure, dark region indicates newly formed metal palladium compounds between Pd metal and recessed barrier layer interface. As the dotted line indicates in the figure 4.3, the new schematic band diagram of the thinned barrier layer can be seen to cause positive shift of the threshold voltage and the capacitance increase due to the metallic compound formation at the interface during the annealing process. The carrier density of $2.0 \times 10^{11} \text{ cm}^{-2}$ and the mobility of $18,659 \text{ cm}^2\text{V}^{-1}\text{s}^{-1}$ were measured by van der Pauw method at room temperature. As source and drain ohmic contact of these devices, Au/Ge/Au/Pd/Au 300/400/300/150/500 Å layer were evaporated by electron-beam evaporator and annealed by rapid thermal annealing at 420°C for 75 s. Before formation of the gate, gate recess etching was performed by wet chemical etching using phosphoric acid

($\text{H}_3\text{PO}_4:\text{H}_2\text{O}_2:\text{H}_2\text{O}=1:1:30$) at 15°C . Gate metal stack of Pd/Ti/Au $200/200/500 \text{ \AA}$ was deposited and annealed for 5 min in N_2 ambient. Three different annealing temperatures, i.e., 200, 250, 300 $^\circ\text{C}$, were chosen for each device. During the anneal process, formation of Pd_5As , Pd_4Al_3 and so on are suggested to be formed at interface of Pd and $\text{In}_{0.52}\text{Al}_{0.48}\text{As}$ barrier-layer. [4]

Source	Gate	Drain
$\text{In}_{0.52}\text{Al}_{0.48}\text{As}$	Alloy barrier	500 \AA
Si	δ -dope	$1.0 \times 10^{12} \text{ cm}^{-2}$
$\text{In}_{0.52}\text{Al}_{0.48}\text{As}$	spacer	100 \AA
$\text{In}_{0.53}\text{Ga}_{0.47}\text{As}$	sub-channel	50 \AA
$\text{In}_{0.81}\text{Ga}_{0.19}\text{As}$	channel	50 \AA
$\text{In}_{0.53}\text{Ga}_{0.47}\text{As}$	sub-channel	50 \AA
$\text{In}_{0.52}\text{Al}_{0.48}\text{As}$	spacer	100 \AA
Si	δ -dope	$5.0 \times 10^{11} \text{ cm}^{-2}$
$\text{In}_{0.52}\text{Al}_{0.48}\text{As}$	buffer	$0.8 \mu\text{m}$
InP	buffer	$0.3 \mu\text{m}$
InP (100) substrate		

Figure 4. 1 Schematic heterostructure diagram of the InGaAs-based HEMT transistor. After rapid thermal anneal, the drain and source electrode reach to channel is indicated with dotted line.

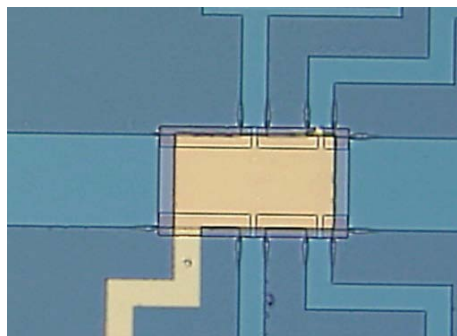


Figure 4. 2 A fabricated Hall bars with 50 and 150 μm of gate width and length.

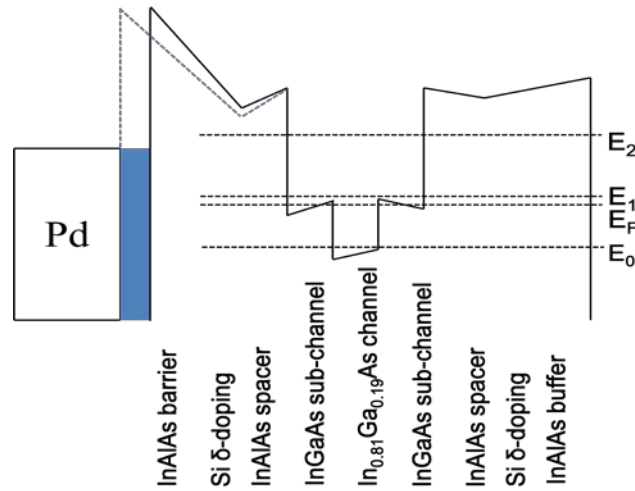


Figure 4. 3 A schematic of conduction diagram of the Schottky junction before (dotted line) and after annealing (solid line). Dark area indicates metallic palladium compounds formed after anneal.

4.3 Results and Discussion

The fabricated devices were analyzed by electrical measurements by analyzing Schottky characteristics and drain to source current-gate to source voltage (I_{ds} - V_{gs}) characteristics. The value of Schottky barrier height was estimated by the thermionic diffusion theory. The appropriate Richardson constant was derived from effective mass. [7-8] Figure 4.4 shows drain to source current and transconductance dependence on gate voltage before and after the anneal at 250°C for 5 min when drain to source voltage was 1.0 V. It indicates that the transconductance was enhanced and threshold voltage was shifted over anneal, which barrier-layer width was decreased. Prior to the Schottky anneal, this device had -0.52 V of threshold voltage and 650 $\mu\text{S}/\text{mm}$ of maximum transconductance. After Schottky anneal, the device performances changed to be -0.38 V of threshold voltage and 700 $\mu\text{S}/\text{mm}$ of maximum transconductance. The depth of the alloy layer was estimated to be 50 Å by transconductance peak shift before and after annealing process. Figure 4.5 shows Schottky characteristics of the present device. Ideality factor was found to be 1.03 and 1.05 before and after anneal, respectively. The Schottky barrier height of this device was 0.68 eV both before and after anneals. The carrier mobility after annealing was measured to be 18,841 $\text{cm}^2\text{V}^{-1}\text{s}^{-1}$ by Hall-effect

measurement. It indicates that the Schottky characteristic of Pd-gate was not degraded over the annealing process. Annealing temperature dependence of threshold voltage shift, Schottky barrier height, and ideality factor are shown in Fig. 4.6(a), (b), and (c), respectively. The horizontal axis of Fig. 4.6 corresponds to annealing temperature. This gate recess etching time of the samples shown in Fig. 4.6 was different from that of Fig. 4.5. The estimated barrier layer thickness in Fig. 4. after gate recess was 300 Å by the corresponding etching rate, while that of samples in Fig. 4.3 was 400 Å. The barrier thickness difference of between Fig. 4.5 and 4.6 can be verified by the threshold voltage differences. At 250°C for 5 min annealing, threshold voltage shift of Fig. 4.4 and 4.5 were 0.13 and 0.2 V, respectively. The threshold voltage shift in Fig. 4.6 (a) was around 0.15, 0.22, and 0.3 V when annealed at 200, 250, and 300°C, respectively, which was linearly proportional to annealing temperature. In other words, the Schottky interface was found to progress linearly with annealing temperature. In Fig. 4.6 (c), shifted value of ideality factor of each device is plotted against annealing temperature. Before anneal, ideality factor of most of the devices distributed at around 1.2 to 1.3. After anneal, the values were not degraded, except samples annealed at 300°C. The deterioration is presumably caused by the increased gate leakage current due to tunneling through thinned barrier-layer as thin as 225 Å estimated by the threshold voltage shift and reaction rate.

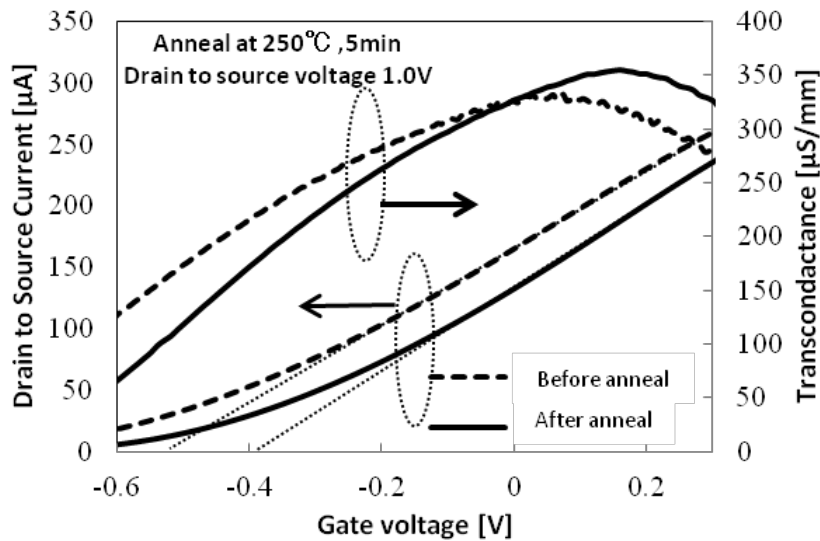


Figure 4. 4 Drain and gate current characteristics of one of the fabricated devices. The

transconductance enhancement and the threshold voltage increase can be seen after anneal. The barrier thickness shrinkage was estimated to be 50 Å.

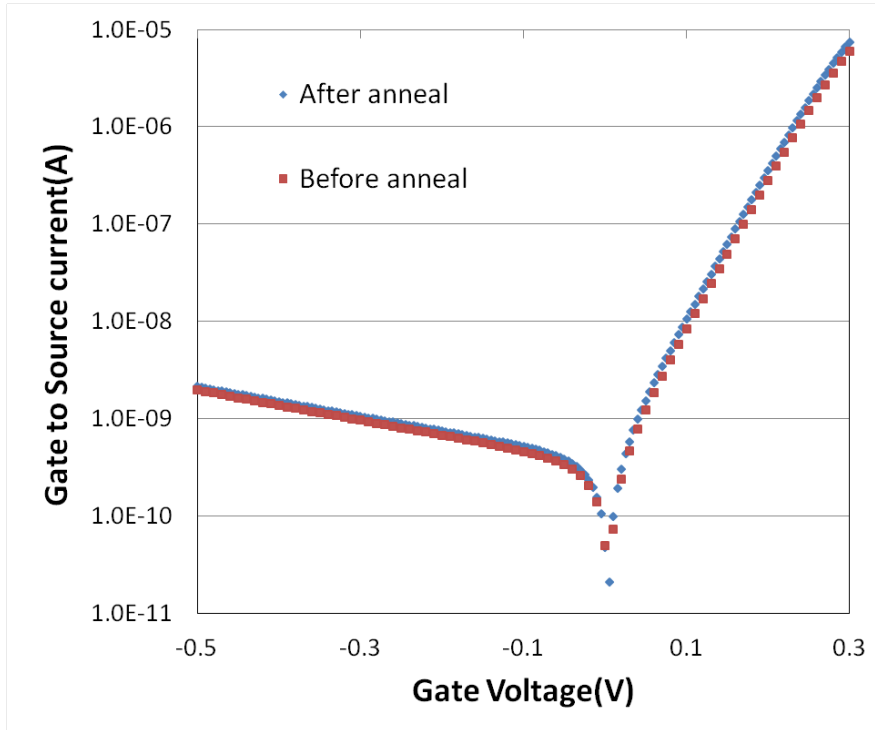
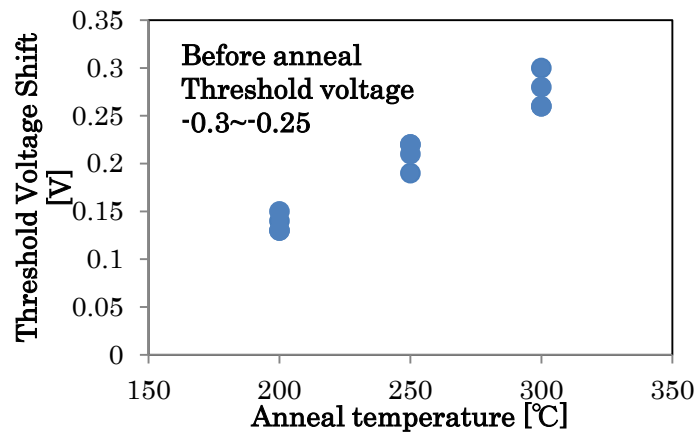


Figure 4. 5 Schottky diode characteristics of the device. It shows that 0.68 eV of Schottky barrier height and around 1.0 of Ideality factor was not deteriorated during the anneal.



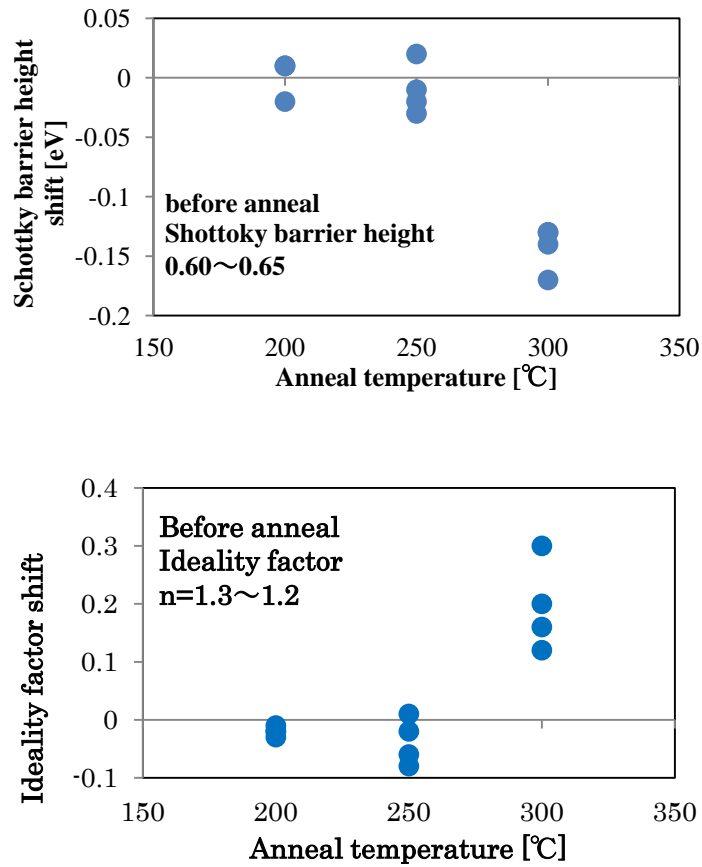


Figure 4. 6 Threshold voltage shift (a), Schottky barrier height shift (b), and Ideality factor shift (c) are illustrated as function of annealing temperature. The threshold voltage shift (a) is seen to be proportional to annealing temperature. The Schottky barrier height shift (b) and Ideality factor shift (c) were not degraded, exempt for 300°C. Because gate leak current was increased considerably.

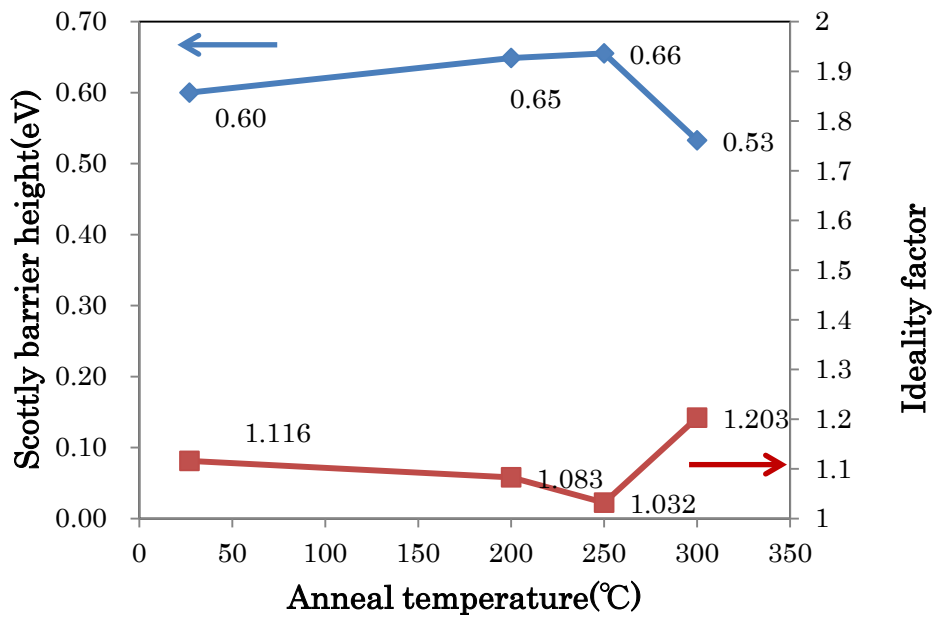


Figure 4. 7 The Schottky barrier height and ideality factor dependant on annealing temperature.

Bibliography

- [1] E. Zanoni, A. Callegari, C. Canali, F. Fantini, H. Hartnagel, F. Magistrali, A. Pacagnela, and M. Vanzi, *Qual. Reliab. Eng. Int.* 6, 29 (1990)
- [2] N. Toyoda, *Proc. 14th Conf. Solid State Device*, Tokyo, 1982, *Jpn. J. Appl. Phys.* 22, 345 (1983).
- [3] K. Yoh, H. Takeuchi, H. Hasegawa, S. Izumiya and M. Inoue, *Solid-State Electron.* 38 1611 (1995).
- [4] A. Mahajan, M. Arafa, P. Fay, C. Caneau, and I. Adesida, *IEEE Trans. Electron Devices* 45, 2423 (1998).
- [5] H. C. Chiu, C. W. Yang, C. H. Chen, C. K. Lin, J. S. Fu, H. Y. Tu, and S. F. Tang, *Microelectron. Reliab.* 50, 847 (2010).
- [6] H. F. Chuang, C. P. Lee, C. M. Tsai, D. C. Liu, J. S. Tsang and J. C. Fan, *J. Appl. Phys.* 83, 366 (1998).
- [7] E. D. Palik and R. F. Wallis, *Phys. Rev.* 123, 131 (1961).
- [8] D. J. Stukel and R. N. Euwema, *Phys. Rev.* 188, 1193 (1969).

Chapter 5

Spin injection into InAs Quantum well

In this section, the experimental electrical spin injection into InAs quantum well is described. First, several layer structure was designed and analyzed as regards enhancement of the strength spin orbit coupling. A clear enhancement of the spin orbit interaction was observed with engineered InAs QW. For spin injection measurement, nonlocal lateral spin valves were fabricated with n-Si and InAs QW for comparison. Then, the spin polarization was evaluated via spin valve and Hanle effect measurement.

5.1 InAs quantum well structure

5.1.1 InAs quantum well layer design

Strong spin orbit coupling is necessary for achieving a short channel length for spin FET. In this section, layer structures in InAs-based heterostructure were investigated for enhancing the spin orbit coupling. These four different layer structures were prepared as shown in Fig. 5.1.1 (a) – (d). Then, the strength of spin orbit coupling was measured by using Shuvnikov de-Haas oscillation at low temperature.

In _{0.53} Ga _{0.47} As	10 nm
In _{0.52} Al _{0.48} As	50 nm
Si doping	$1.6 \times 10^{12} \text{ cm}^{-2}$
In _{0.52} Al _{0.48} As	10 nm
In _{0.53} Ga _{0.47} As	5 nm
In _{0.81} Ga _{0.20} As	5 nm
In _{0.53} Ga _{0.47} As	5 nm
In _{0.52} Al _{0.48} As	0.8 μm
InP	0.3 μm
S.I. InP (100) substrate	

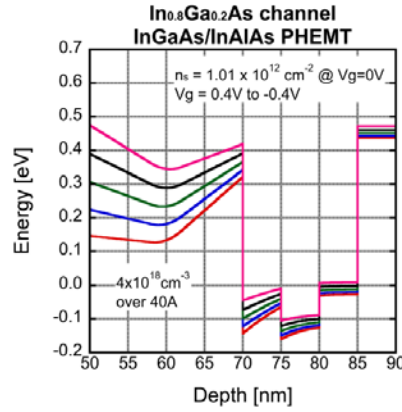


Figure 5.1.1a Normal In_{0.8}Ga_{0.2}As-based heterostructure.

In _{0.53} Ga _{0.47} As	10 nm
n-In _{0.53} Ga _{0.47} As	10 nm $1.6 \times 10^{18} \text{ cm}^{-2}$
In _{0.52} Al _{0.48} As	60 nm
In _{0.53} Ga _{0.47} As	5 nm
In _{0.81} Ga _{0.20} As	5 nm
In _{0.53} Ga _{0.47} As	5 nm
In _{0.52} Al _{0.48} As	10 nm
Si doping	$1.2 \times 10^{12} \text{ cm}^{-2}$
In _{0.52} Al _{0.48} As	0.8 μm
InP	0.3 μm
S.I. InP (100) substrate	

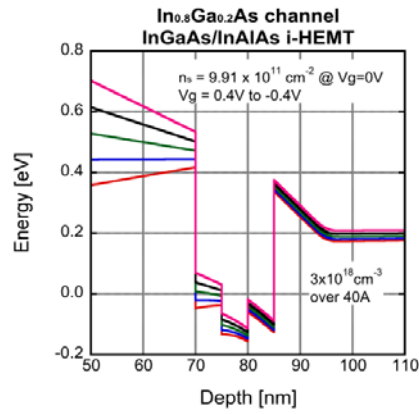


Figure 5.1.1b Inverted In_{0.8}Ga_{0.2}As -based heterostructure.

In _{0.53} Ga _{0.47} As	10 nm
In _{0.52} Al _{0.48} As	50 nm
Si doping	$1.2 \times 10^{12} \text{ cm}^{-2}$
In _{0.52} Al _{0.48} As	10 nm
In _{0.53} Ga _{0.47} As	5 nm
In _{0.81} Ga _{0.20} As	5 nm
In _{0.53} Ga _{0.47} As	5 nm
In _{0.52} Al _{0.48} As	10 nm
Si doping	$5.0 \times 10^{11} \text{ cm}^{-2}$
In _{0.52} Al _{0.48} As	0.8 μm
InP	0.3 μm
S.I. InP (100) substrate	

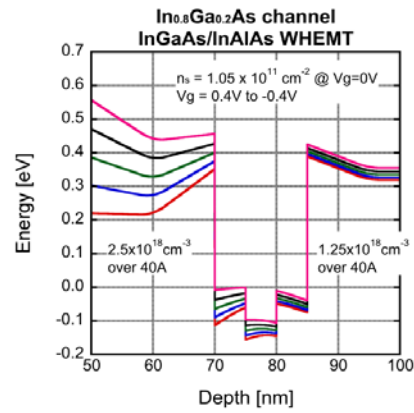


Figure 5.1.1c Double doped In_{0.8}Ga_{0.2}As -based heterostructure.

In _{0.53} Ga _{0.47} As	10 nm
In _{0.52} Al _{0.48} As	50 nm
In _{0.53} Ga _{0.47} As	1.8 nm
InAs	4.1 nm
In _{0.53} Ga _{0.47} As	5.6 nm
In _{0.52} Al _{0.48} As	10 nm
Si doping	$1.2 \times 10^{12} \text{ cm}^{-2}$
In _{0.52} Al _{0.48} As	0.8 μm
InP	0.3 μm
S.I. InP (100) substrate	

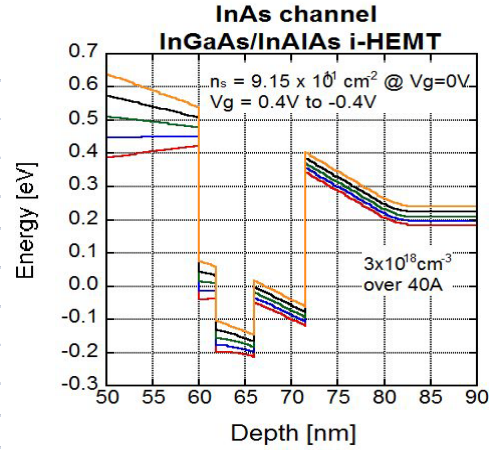


Figure 5.1.1d Inverted InAs-based heterostructure.

The table 5.1.2 show results of the electrical characteristics and spin orbit coupling strength (SOI strength) in each wafers. The wafer d indicated the strongest SOI strength and lower carrier mobility compare to the others. As considered to the narrower quantum well width ($\sim 12 \text{ nm}$) in wafer d, the carrier density inside band offset (depleted region) become relatively higher. These results clearly indicate the effectiveness of the inserted abrupt band discontinuities in the middle of the QWs for the enhancement of Rashba effect, as reported before [1-3]. In the spin injection experiment into an InAs quantum well, the wafer d was used for fabricating a lateral spin valves

	a	b	c	d
Mobility (cm^2/Vs)	63200	154000	252000	28000
Carrier density ($/\text{cm}^2$)	0.9	1.28	0.85	1.5
SOI strength 10^{12} eVm	10	11	9.3	25

Table 5.1.2 Electrical transfer characteristics and SOI strength data.

5.2 Spin injection into n-Si

First, spin injection and spin accumulation in highly doped n-type Si was investigated for confirming the tunneling barrier effectiveness before InAs quantum well. Spin transfer characteristics was characterized by non-local measurements with MgO tunnel barrier. The measurement results indicated that the MgO samples showed nonlocal spin valve signal, whereas samples without MgO did not show it. However, it remarked unequivocal evidence of spin accumulation inside Si in three terminals Hanle

measurement, while maintaining symmetric characteristics in magnetic field. In this report, we have discussed the spin accumulation effects on the two types of interface structures.

5.2.1 Device fabrication and electrical characterization

Fabricated device structure consists of 50 nm-thick phosphorus-doped silicon channel layer, 150 nm of SiO₂, p-type Si substrate, as shown in Fig. 5.2.1. The carrier density of the channel was obtained by Hall measurement to be approximately $3 \times 10^{19} \text{ cm}^{-3}$ at room temperature. Pattern definition of all fabrication process was conducted by electron beam lithography and reactive ion etching (CF₄ and O₂ gas). For Ohmic contact, Ni electrodes were stacked with electron beam evaporator followed rapid thermal annealing to silicide. After eliminating native oxide by buffered hydrofluoric acid, Fe (15 nm) or NiFe/MgO (30/2 nm) were stacked by electron beam evaporator in the ultra high vacuum (UHV) chamber lower than 1×10^{-9} Torr. Then, Au cap layer was deposited for preventing further oxidation. For enhanced MgO crystalline, annealing process were employed only for MgO samples at 300 °C for 60 min in UHV chamber. The measurement configuration is shown in Fig. 5.2.1. the current-voltage characteristics between contact 1 and 2 indicated linear behavior and the contact area products were estimated to be $2.3 \text{ k}\Omega \mu\text{m}^2$ at 1.4 K.

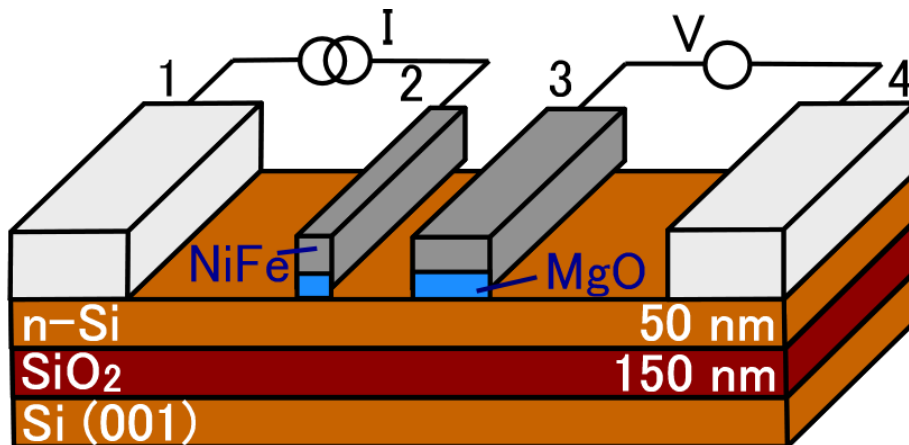


Figure 5.2.1 Schematics of fabricated nonlocal lateral spin valves. The device consist 50 μm of mesa isolation width and 0.5 and 0.8 μm of ferromagnetic electrodes. External magnetic field is aligned to long axis of ferromagnetic electrodes.

5.2.2 Spin valve measurement

Magnetoconductance measurement was conducted with nonlocal lateral spin valves geometry. The measurement results of nonlocal signal for 1 mA of biased current are shown in Fig. 5.2.2 (a). External magnetic field (B_{ext}) was applied parallel to longitudinal direction of FM electrodes from -800 to 800 Gauss in order to obtain nonlocal voltage change clearly. When the magnetic field was swept, the peaks of nonlocal signals of 30 μV was detected at $B_{ext}=\pm 170$ Gauss. In addition to this result, spatial FM electrodes dependence of nonlocal voltage was shown in Fig. 5.2.2 (b) together with the fitting based on the equation $V_{NL}=RP^2(IL_{sd}/S)\exp(-L/L_{sd})$, where R is resistivity of the Si channel, P is the spin polarization, S is the cross sectional area of channel and L_{sd} is the spin diffusion length. The spin diffusion length of 1.66 μm was obtained with the fitting curve. The spin relaxation time was estimated to be 7.45 ns given by $\tau_s=DL_{sd}^2$, where τ_s is the spin relaxation time, D is the diffusion constant. These data were consistent with previously reports. [1] The nonlocal amplitude was linearly proportional to biased current according to theory in Fig. 5.2.2 (c). [2] It is reasonable evidence that the spin transfer is occurred inside Si channel.

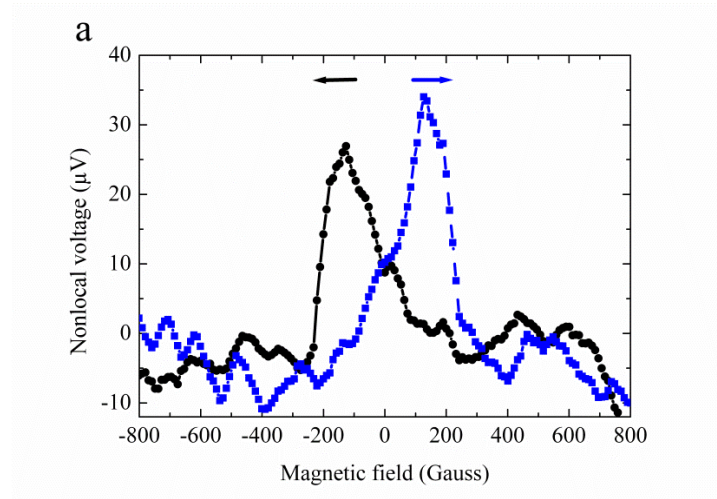


Figure 5.2.2a Result of a nonlocal spin injection (NiFe/MgO/n-Si) at 1.4 K. The data were taken for the device of $L=1.4 \mu\text{m}$, while the biased current fixed to $I=1 \text{ mA}$. The offset of nonlocal voltage was excluded.

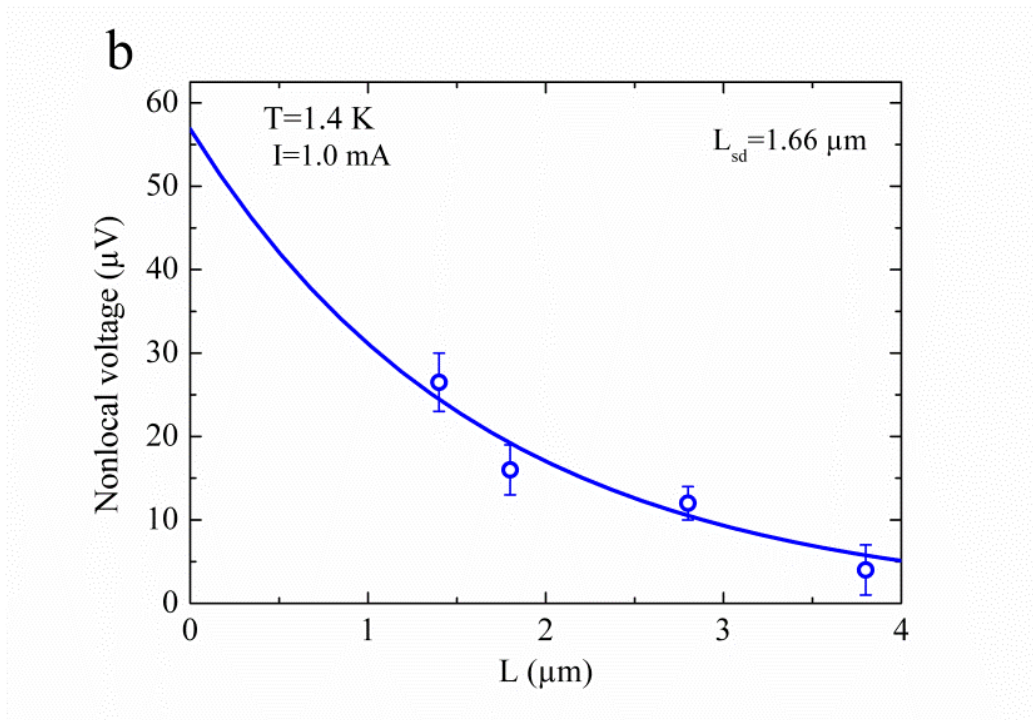


Figure 5.2.2b Spatial FM electrodes dependence of nonlocal voltage at 1.4 K, when biased current set to be 1 mA. The line indicates the exponential decay fitting curve.

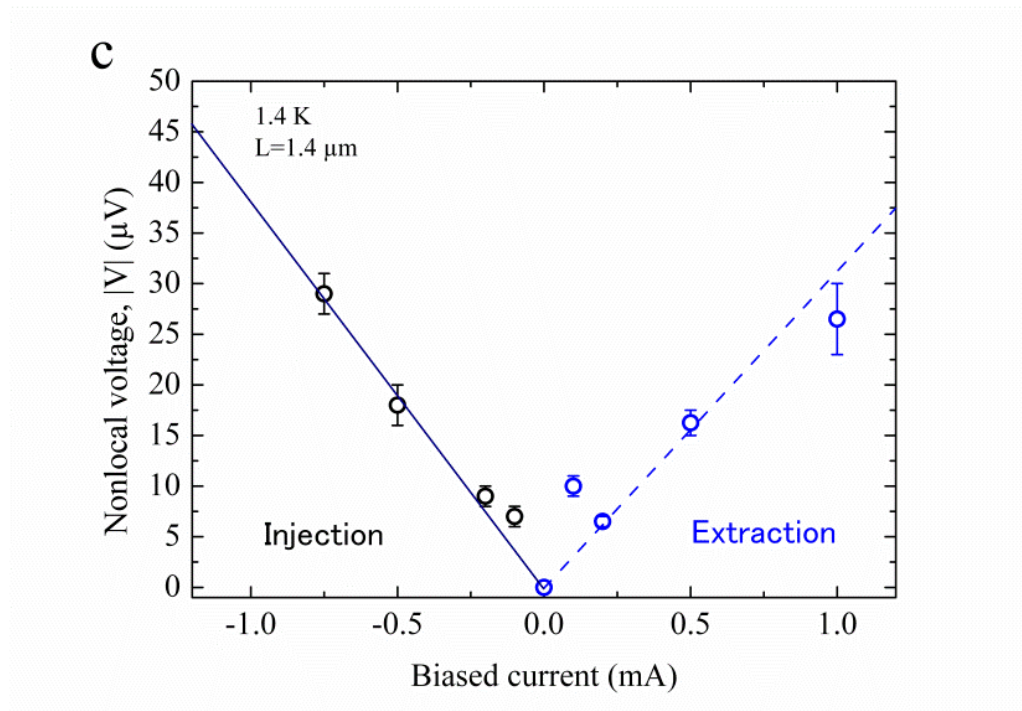


Figure 5.2.2c Bias dependence of nonlocal voltage at 1.4 K for $L=1.4\text{ }\mu\text{m}$ sample. The positive (negative) current direction indicate spin extraction (injection) direction.

5.2.3 Hanle effect measurement in Fe/n-Si

Nonlocal spin signals with no tunneling barrier sample (Fe/n-Si) was not observed, probably because of an accumulated spin potential in FM detector, which is expected to be weak compared with NiFe/MgO/n-Si sample. For this reason, three terminals Hanle measurement was conducted to observe the spin accumulation in zero length. Schematics of fabricated sample for three terminals Hanle was shown in Fig. 5.2.3. The SOI wafer is the same as shown in Fig. 5.2.1. The contact pad size is 150 μm in width and 200 μm in length, respectively. The contact pad separation of 50 μm is enough to cause diffusive state.

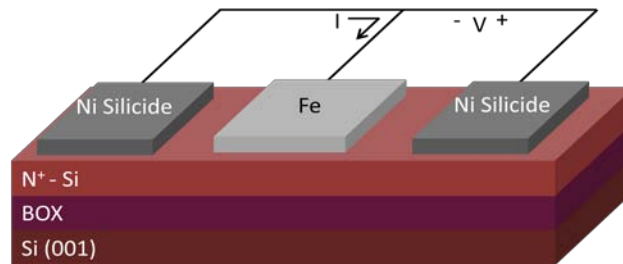


Figure 5.2.3 Schematics of a three terminals Hanle configuration in Fe/n-Si. 150 \times 200 μm^2 of electrodes size and 50 μm channel length (between contacts).

The results of 3T Hanle measurement are exhibited in Fig. 5.2.4 with various constant current conditions. The Hanle line shape should be approximated with Lorentzian function given by $V(B)=V(0)/(1+\omega L^2\tau s^2)$, where ωL is the Lamor spin precession. As see in Fig. 5.2.4, two type of Hanle-like signal were observed to overlap and the shape indicated symmetric with biased current direction (injection and extract direction). The spin relaxation times were estimated to be 3.4 ns of narrower peaks for I=3 mA and 0.4 ns of wider peaks for 1 mA, respectively. It is clear evidence that the narrower peaks are originated from Si as referred from the NL spin relaxation time of 7.45 ns, which spin is relaxed inside Si channel against perpendicular magnetic fields. We further note that the amplitudes of narrower peak were linearly proportional to biased current as shown in Fig. 5.2.6. For the broader peaks, the amplitudes were obtained to be particular characteristics with biased current. In this narrow Schottky barrier between Fe and n-Si,

tunneling contact resistance would be intensely sensitive to band bending of biased field. The disappearance of broader peak at high bias situation suggests tunneling resistance related origin which is consistent with literature, Uemura et al. [3] Accordingly, a observed authentic Hanle signal was to be unleashed from a spurious Hanle-type signals in this specific regime.

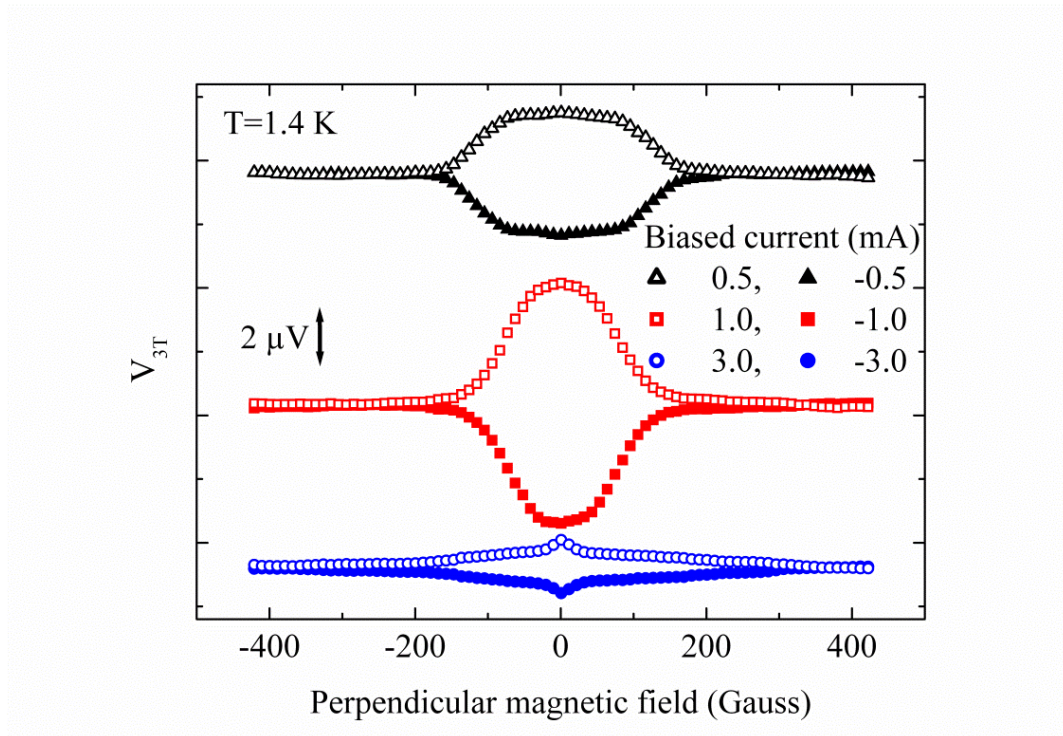


Figure 5.2.4 Result of three terminal Hanle measurement in Fe/n-Si at 1.4 K. Perpendicular external magnetic field was swept from -400 to 400 Gauss, where the bias current was set to $I=\pm 0.5$, ± 1 and ± 3 mA.

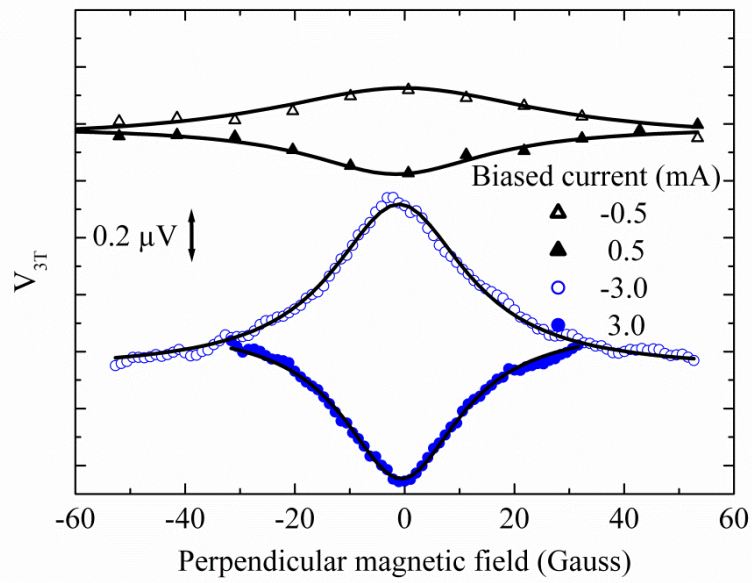


Figure 5.2.5 The narrower peaks were shown in $I=\pm 0.5$ and ± 3 mA including the fitting of Lorentzian function (lines).

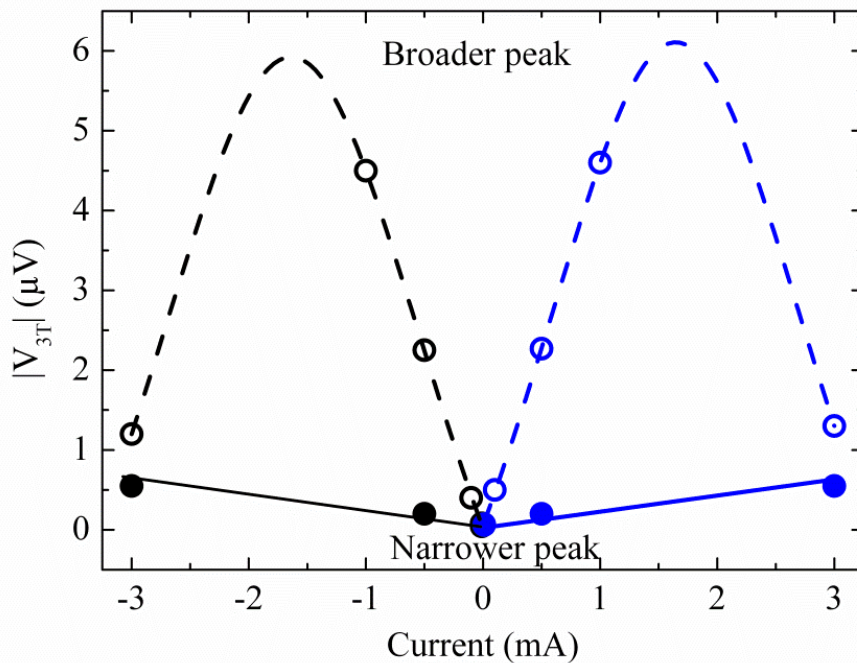


Figure 5.2.6 3T Hanle amplitude as a function of biased current. The broader and narrower peaks showed distinct characteristics.

5.2.3 Conclusion

We have demonstrated spin injection with situation of NiFe/MgO/n-Si and Fe/n-Si to reveal the reliability of the 3T Hanle measurement. NL spin accumulation was observed in NiFe/MgO/n-Si clearly. The estimated spin transport properties were 1.66 μm of spin diffusion length and 7.45 ns of spin relaxation time, respectively. In the 3T Hanle measurement, we have observed the broader and narrower Hanle-like signals in Fe/n-Si simultaneously, and the broader peak was strongly diminished at high bias situation. Evidently, typical 3T Hanle-like signal was originated from magnetic-field-dependent tunnel resistance.

5.3 Spin injection into InAs quantum well

5.3.1 Device structure

According the previous NiFe/MgO/n-Si data, we have fabricated a lateral spin transport device with a NiFe/MgO spin injector/detector as shown in Fig. 5.3.1(a). The transport channel consists of an $\text{In}_{0.53}\text{Ga}_{0.47}\text{As}/\text{InAs}/\text{In}_{0.53}\text{Ga}_{0.47}\text{As}$ QW. A layer structure consisting of (from the substrate side) a 300/800-nm-thick $\text{InP}/\text{In}_{0.52}\text{Al}_{0.48}\text{As}$ buffer layer, a Si δ -doping layer with a sheet concentration of $1.2 \times 10^{12} \text{ cm}^{-2}$, a 10-nm-thick $\text{In}_{0.52}\text{Al}_{0.48}\text{As}$ spacer layer, a 5.6-nm-thick $\text{In}_{0.53}\text{Ga}_{0.47}\text{As}$ sub-channel, a 4.1-nm-thick InAs main channel, a 1.8-nm-thick $\text{In}_{0.53}\text{Ga}_{0.47}\text{As}$ sub-channel, a 50-nm-thick $\text{In}_{0.52}\text{Al}_{0.48}\text{As}$ barrier layer and a 10-nm-thick $\text{In}_{0.53}\text{Ga}_{0.47}\text{As}$ capping layer was grown on a semi-insulating InP (001) substrate. Figure 5.3.1 (b) shows a calculated energy band structure of the InAs QW. The InAs QW is close to the InGaAs/InAlAs heterointerface so that electrons experience a large electric field arising from the InGaAs/InAsAs band offset, which induces the large Rashba SOI. For a spin injection device, a 50- μm -wide channel was constructed by wet chemical etching aligned along the [110] direction. The FM electrode patterns for a spin injector and a detector were defined for 0.2- and 0.4- μm widths using electron beam lithography. A $\text{Ni}_{81}\text{Fe}_{19}$ (70 nm)/MgO (2) stack was deposited by an electron beam evaporator in an ultra-high vacuum chamber on the InAs channel directly after wet chemical etching of the top InGaAs/InAlAs (/InGaAs) barrier

layers. A sample with NiFe/In_{0.53}Ga_{0.47}As/InAs Schottky tunnel junctions was also fabricated for comparison.

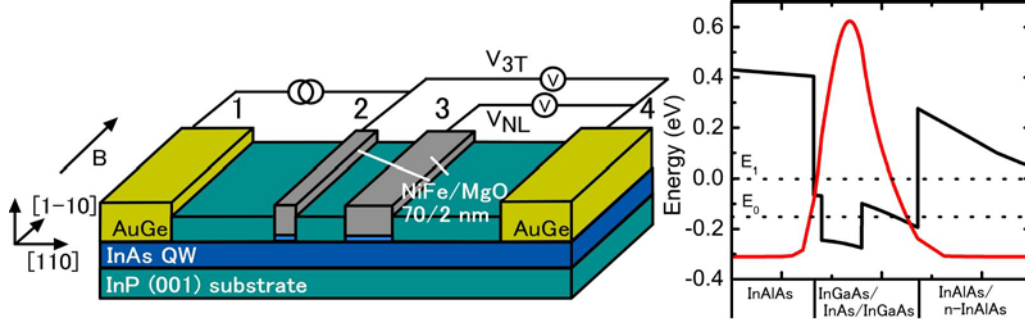


Figure 5.3.1 Schematic diagram of a four-terminal lateral transport device for nonlocal spin-valve measurements and a band simulation for the semiconductor channel. A wide channel of 50 μm was formed by wet chemical etching. After the top barrier layers were etched down to the InAs channel layer, NiFe/MgO was stacked. The width of the spin injector and detector (NiFe/MgO) were to be 0.2 and 0.4 μm . For spin valve measurements, the magnetic field was swept in the long distance [1-10] direction of the electrodes. NL voltage was detected between 3 and 4, while constant current was supplied from 2 to 1. To measure in-plane magnetoresistance of the injector (detector) contact, a three-terminal voltage was sensed between 2 (3) and 4.

5.3.2 Electrical characteristics

The electrical transport properties were characterized by Hall effect measurement, which yielded mobility of $2.0 \times 10^4 \text{ cm}^2/\text{Vs}$, sheet carrier density (n_s) of $1.5 \times 10^{12} \text{ cm}^{-2}$, and sheet resistance (R_s) of $300 \text{ }\Omega/\text{sq.}$ at 1.4 K. The SOI parameter α was observed to be $\sim 23 \times 10^{-12} \text{ eVm}$ at 1.4 K as determined by Shubnikov-de Haas oscillation and its waveform analysis by the maximum entropy method of fast Fourier transform. This value is approximately 2.6 times larger than the value in the literature [4], possibly due to a high carrier density at the InAlAs/InGaAs band offset, although the carrier mobility would become relatively lower. This strong SOI parameter leads to a short spin precession length of approximately 340 nm over the mean free path of 600 nm; that is, the spin relaxation due to the D'yakonov-Perel' mechanism can be avoided in the case of a quasi-one-dimensional ballistic transport regime [5-6]. This value meets a

requirement for realizing a Datta-Das spin transistor. Figure 5.3.2 shows the resistance-area product ($R \cdot A$) as a function of bias voltage for a NiFe/MgO/InAs tunnel junction at room temperature and 1.4 K. A clear tunneling behavior was observed. This contrasted with the result for a NiFe/InGaAs/InAs junction, which showed ideal ohmic behavior (*not shown*). The value of $R \cdot A$ for NiFe/MgO/InAs in the vicinity of zero-bias was approximately $2 \text{ k}\Omega \mu\text{m}^2$, a value two orders of magnitude higher than that of NiFe/InGaAs/InAs ($< 20 \text{ }\Omega \mu\text{m}^2$). The relatively low $R \cdot A$ values observed in the NiFe/InGaAs/InAs junction are consistent with the literature [9].

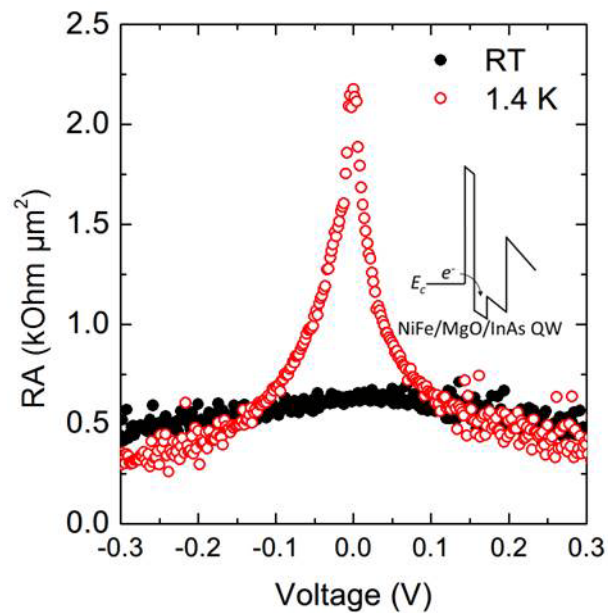


Figure 5.3.2 RA-voltage characteristics in the NiFe/MgO/InAs QW at RT (closed circle) and 1.4 K (open circle). A schematic diagram of the conduction band near the NiFe/MgO/InAs interface is shown in the inset.

5.3.4 Spin valve measurement

Figures 5.3.3(a) and (b) show typical results of the NL spin-valve measurement at 1.4 K for (a) NiFe/MgO/InAs and (b) NiFe/InGaAs/InAs. The spacing between injector (terminal 2) and detector (terminal 3) in the NL measurement was $0.7 \text{ }\mu\text{m}$. For the sample with an MgO barrier, clear voltage peaks were obtained at 10 mT and at -3 mT upon positive and negative sweeps of the external magnetic field, respectively. By contrast, for the sample without an MgO barrier the NL signal was not reproducible

among the junctions in the wafer, and no clear NL signal was observed, indicating no spin injection. In the NL measurement for the sample with an MgO barrier, a background resistance of approximately 22Ω was detected possibly due to unintentional electrical charge flow into the detector circuit of the NL voltage. This electrical charge flow may have affected the change of the NL signal if there was any magnetoresistance (MR) effect, such as anisotropic magnetoresistance (AMR) of the FM electrode or tunneling AMR [7-10] of the tunnel junction, from the injector contact. To verify whether this was the case, we measured the MR of the injector contact using a three-terminal (3T) geometry, in which a constant current of $100 \mu\text{A}$ was supplied between terminals 2 and 1, and the voltage between terminals 2 and 4 was detected under sweeping by an in-plane magnetic field. The MR of detector contact 3 was similarly measured. The results are shown in Figs. 5.3.3(c) - (f). All data were normalized by the value at zero magnetic field. The 3T signal for NiFe/InGaAs/InAs showed a spin-valve-like signal, as shown in Figs. 5.3.3(d) and (f), with an MR ratio of approximately 0.04% due to AMR of the NiFe electrode, while those for NiFe/MgO/InAs showed no such AMR signal (Figs. 5.3.3(c) and (e)). This is because the tunnel resistance of the MgO barrier is much higher than that of the NiFe electrode. The junction resistance of NiFe/MgO/InAs was almost constant against the in-plane magnetic field with an MR ratio of less than 0.008%. Thus, we concluded that the NL voltage change observed for the sample with an MgO barrier originated from the spin-valve effect; i.e., switching between the P and AP states for the relative magnetization configuration between the injector and detector contacts. This result indicates a clear spin injection from NiFe into an InAs QW through an MgO tunnel barrier.

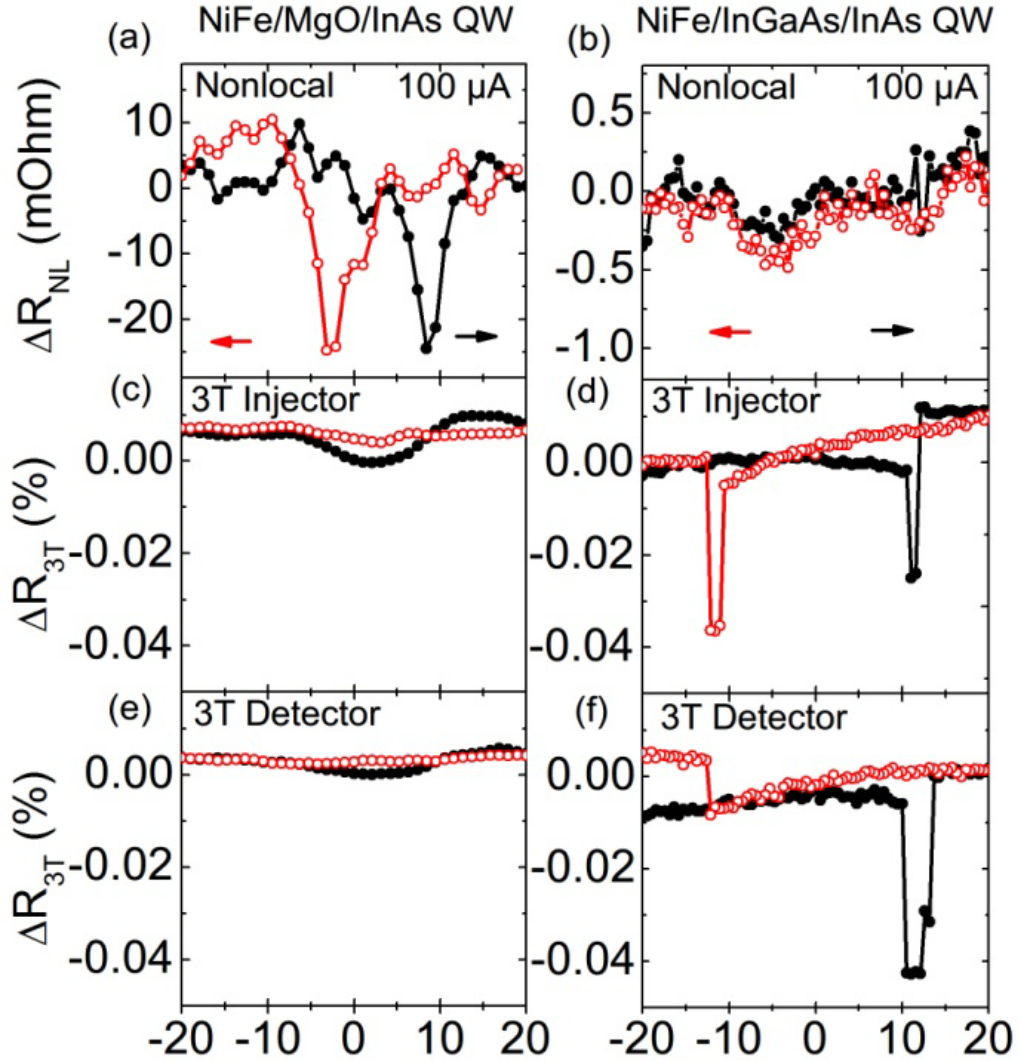


Figure 5.3.3 (a), (b). Non-local spin-valve signals for (a) NiFe/MgO/InAs and (b) NiFe/InGaAs/InAs at 1.4 K. The closed circle (open circle) represents positive (negative) direction sweep of the external magnetic field along the longitudinal axis of ferromagnetic electrodes. The slightly asymmetric behavior of the nonlocal signal with respect to the polarity of the magnetic field is due to the existence of the residual field from the superconducting magnet. A background signal was subtracted. (c), (d). In-plane magnetoresistance for injector contact for (c) NiFe/MgO/InAs and (d) NiFe/InGaAs/InAs. (e), (f). In-plane magnetoresistance for detector contact for (e) NiFe/MgO/InAs and (f) NiFe/InGaAs/InAs.

Figure 5.3.4 shows the L dependence of ΔR_{NL} for the sample with an MgO barrier,

where L is the spacing between the injector and detector contact, and ΔR_{NL} is the NL resistance change defined as $R_{NL}^P - R_{NL}^{AP}$, where $R_{NL}^{P(AP)}$ is NL resistance for the P (AP) configuration. Based on the conventional one-dimensional spin diffusion model, ΔR_{NL} is given by [11]

$$\Delta R_{NL} = \frac{4R_{SC} \left[\frac{P_I}{1-P_I^2} \left(\frac{R_I}{R_{SC}} \right) + \frac{P_{FM}}{1-P_{FM}^2} \left(\frac{R_{FM}}{R_{SC}} \right) \right]^2 \exp\left(-\frac{L}{\lambda_{SC}}\right)}{\left[\frac{2}{1-P_I^2} \left(\frac{R_I}{R_{SC}} \right) + \frac{2}{1-P_{FM}^2} \left(\frac{R_{FM}}{R_{SC}} \right) + 1 \right]^2 - \exp\left(-\frac{2L}{\lambda_{SC}}\right)} \quad (5.3.1)$$

where $P_{I(FM)}$ is spin polarization at the FM/SC interface (FM electrode), $R_{SC(FM)}$ is the spin resistance of SC(FM), R_I is the interface resistance, and λ_{SC} is the spin diffusion length of SC. For the NiFe/MgO/InAs junction, since R_{FM} is approximately four orders of magnitude smaller than R_I , the second term in the square bracket in eq. (5.3.1) is negligible. Through fitting of the L dependence of ΔR_{NL} with eq. (5.3.1), the values of spin polarization P_I and spin diffusion length λ_{SC} in the InAs QW were determined as 8.1% and 1.6 μm , respectively. The spin lifetime τ_S was estimated to be 8.0 ps from $\tau_S = \lambda_{SC}^2/D$, where the diffusion constant, D , was substituted by that extracted from Hall effect measurements assuming that it is independent of spin polarization. The values of λ_{SC} and τ_S are comparable to those previously reported [12]. The obtained value of 1.6 μm for λ_{SC} is about five-times larger than the estimated spin precession length. The λ_{SC} obtained from the spin-valve measurement is a length scale in which the electron spins parallel to the SOI field conserve their spin states, while the spin precession length is a length needed for electron spins perpendicular to the SOI field to rotate by 2π with the SOI field. Thus, both values should be different. Importantly the obtained spin polarization of 8.1% is approximately four times higher than the previous result with NiFe/InGaAs Schottky junctions [14]. To the best of our knowledge, this is the highest value yet reported for spin injection into InAs.

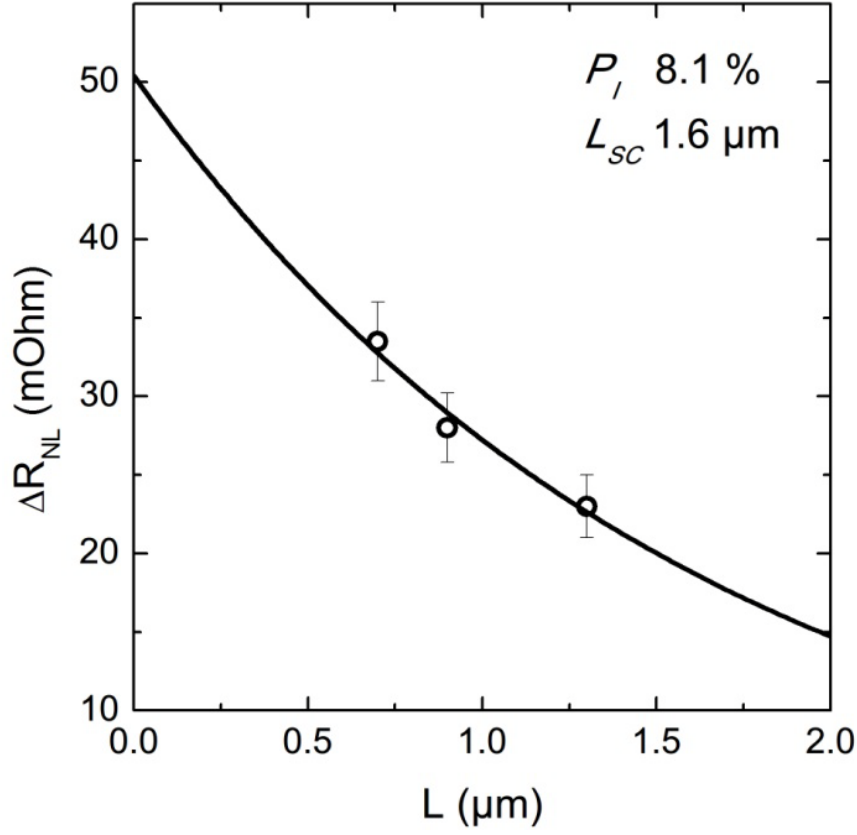


Figure 5.3.4 Magnitude of nonlocal spin-valve signal (ΔR_{NL}) for NiFe/MgO/InAs as a function of spacing (L) between ferromagnetic electrodes. The solid line indicates fitting according to eq. (5.3.1).

We will now discuss the effect of MgO insertion on spin injection properties. From eq. (5.3.1), ΔR_{NL} decreases as the ratio R_I/R_{SC} decreases. This is known as the impedance mismatching problem. The values of R_I/R_{SC} at $I = 100 \mu\text{A}$ are approximately 3 and 0.03, respectively, for the samples with and without the MgO barrier. To avoid the conductivity mismatch problem, the junction resistance R_I should be much larger than R_{SC} . If this condition is satisfied, ΔR_{NL} takes the maximum value of ΔR_{NL}^{max} . From eq. (1), ΔR_{NL}^{max} is given by

$$\Delta R_{NL}^{max} = P_I^2 R_{SC} \exp(-L/\lambda_{SC}) \quad (5.3.2)$$

If we introduce $\Delta R_{NL}/\Delta R_{NL}^{max}$ as a measure of the degree of freedom from the impedance mismatch, it is approximately 74% and 0.6%, respectively, for the samples with and without the MgO barrier. Thus, the sample with the MgO barrier is largely free

from the impedance mismatching problem, resulting in a clear NL spin valve signal, while the spin-valve signal for the sample without the MgO barrier greatly decreases below the detection limit due to the impedance mismatching.

STRUCTURE	$R \cdot A$ ($\Omega \cdot \mu\text{m}^2$)	$\Delta R_{NL} / \Delta R_{NL}^{max}$ (%)
NiFe/InGaAs/InAs	< 20	0.6
NiFe/MgO/InAs	2.5×10^3	74

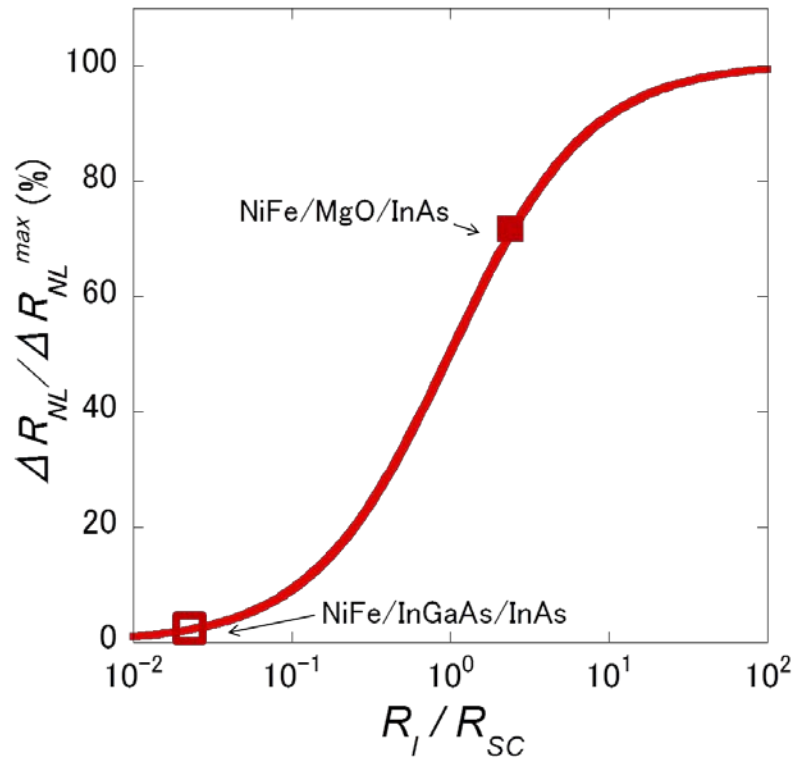


Figure 5.3.5 ΔR_{NL} versus spin resistance mismatch

5.3.5 Hanle effect measurement

Observation of the Hanle precession is the most rigorous evidence of spin injection. In the conventional Hanle effect measurement, application of the out-of-plane magnetic field (B_z) induces Hanle precession. The full-width at half maximum of B_z for the Hanle curve estimated from $B_{1/2} = \hbar / (g^* \mu_B \tau_S)$, where \hbar is the Planck constant divided by 2π , g^* is the effective g -factor (g^* is assumed to be 12 for InAs), and μ_B is the Bohr magneton, is approximately 100 mT. However, no Hanle signal is expected in our sample within ± 100 mT scan for B_z due to the existence of a strong SOI field (B_{SOI}) acting on the

conducting spins. The effective magnetic field from SOIs inside the InAs QW was estimated to be ~ 23 T from $B_{SOI} = (2\alpha k_F)/(g^* \mu_B)$, where $k_F = (2\pi n_s)^{1/2}$ is the Fermi wave number. Since the saturation field of the perpendicular magnetization for NiFe is about 1 T, the magnetization direction of the NiFe electrode is almost unchanged within ± 100 mT scan for B_z . Then, no Hanle precession occurs, because the B_{SOI} , which is dominant for the total magnetic field acting on the electron spins, is parallel to the electron spins. For Hanle precession, application of large B_z comparable to the saturation field of NiFe is necessary so that the spin direction changes from that of B_{SOI} through changing the magnetization direction of the NiFe electrodes. Then the amplitude of the Hanle signal in our sample is estimated to be on the order of several-tens m Ω , since it equals to $\Delta R_{NI}/2$. However we also observed a large background signal in the sample with an MgO barrier as shown in Fig. 5.3.6, the origin of which is still not well understood. The background signal showed almost quadratic dependence on B_z at $|B_z| > 40$ mT, and the change of the background signal was as much as approximately 4 Ω for $0 \leq |B_z| \leq 150$ mT, a value more than two-orders of magnitude larger than that of the estimated Hanle signal. Thus, it is difficult to sense the Hanle signal due to the existence of the large background signal.

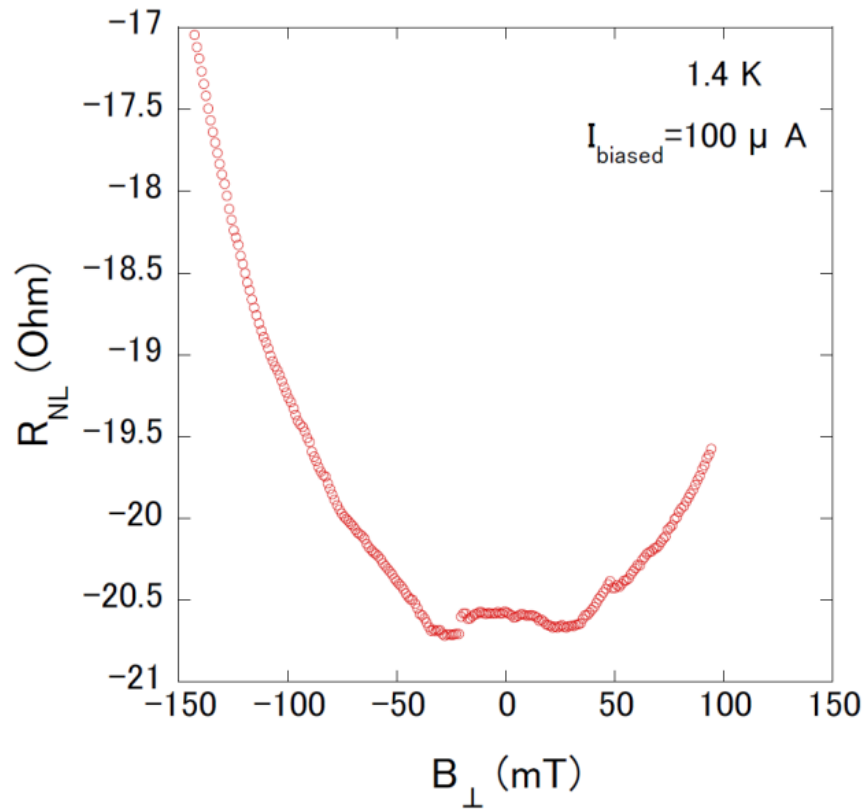


Figure 5.3.6 The Hanle effect measurement in NiFe/MgO/InAs QW.

In summary, we have demonstrated efficient spin injection from NiFe into an InAs QW through an MgO tunnel barrier for potential application to an InAs-based spin transistor. Insertion of an MgO tunneling barrier is an effective way to control the interface resistance for narrow-gap SC systems, enabling effective spin injection.

5.4 Anomalous Hall signals by out-of-plane spin injection from ferromagnet into an InAs quantum well

In this section, I have investigated an InAs channel Hall-bar structure with ferromagnetic spin injector in one of the current terminals. After magnetizing the Fe electrode, spin polarized electrons are injected through the edge of the isolation mesa structure and the anomalous Hall voltage is observed, when even electrons are injected from the ferromagnetic terminal. When the injected spin polarization are maintained stationary, the dynamic nuclear polarization (DNP) based on hyperfine interaction [13] lead to transfer from electron to nuclear spin angular momentum dynamically near the injection edge. If the electron spin is transferred to nuclear spins, effective magnetic field is induced without applying external magnetic field. So far, a number of experiments for application in spintronics have been demonstrated the control of nuclear spin in semiconductors, which have become realistic by various methods such as quantum Hall state edge current [14], creation of spin polarized electrons in quantum dots by irradiating circularly polarized light [15] and nuclear magnetic resonance [16-18], nuclear spin polarization by spin injection from iron to GaAs [19]. We report the control of nuclear spin polarization by vertically polarized spin injection from ferromagnetic metal in InAs heterostructure Hall bar structure.

5.4.1 Device structure

Hall-bar was fabricated on inverted InAs pseudomorphic HEMT structure grown on InP (001) substrate and its schematics is shown in Fig. 5.4.1. The developed device consisting 4.1 nm InAs channel layer in the middle of InGaAs sub-channel layer. The structure consist of 300/800 nm of InP/ $\text{In}_{0.52}\text{Al}_{0.48}\text{As}$ buffer layer, $5.0 \times 10^{11} \text{cm}^{-2}$ of Si δ -doping, 10 nm of $\text{In}_{0.52}\text{Al}_{0.48}\text{As}$ spacer layer, 5.6 nm of $\text{In}_{0.53}\text{Ga}_{0.47}\text{As}$ sub-channel, 5 nm of InAs main channel, 1.8 nm of $\text{In}_{0.53}\text{Ga}_{0.47}\text{As}$ sub-channel, 50 nm of $\text{In}_{0.52}\text{Al}_{0.48}\text{As}$ barrier layer and InGaAs 10 nm cap-layer. The device characteristics indicate 17000 (28000) $\text{cm}^2\text{V}^{-1}\text{s}^{-1}$ of mobility and 0.6 (1.5) $\times 10^{12} \text{cm}^{-2}$ of carrier density at room (helium) temperature. (Figure 5.4.2)

InGaAs	10nm
In _{0.52} Al _{0.48} As	50nm
In _{0.53} Ga _{0.47} As	1.8nm
InAs	4.1nm
In _{0.53} Ga _{0.47} As	5.6nm
In _{0.52} Al _{0.48} As	50nm
Si δ -doping	$1.2 \times 10^{12} \text{cm}^{-2}$
In _{0.52} Al _{0.48} As	0.8 μm
InP (100) substrate	

Figure 5.4.1 Schematic diagram of the InAs heterostructure.

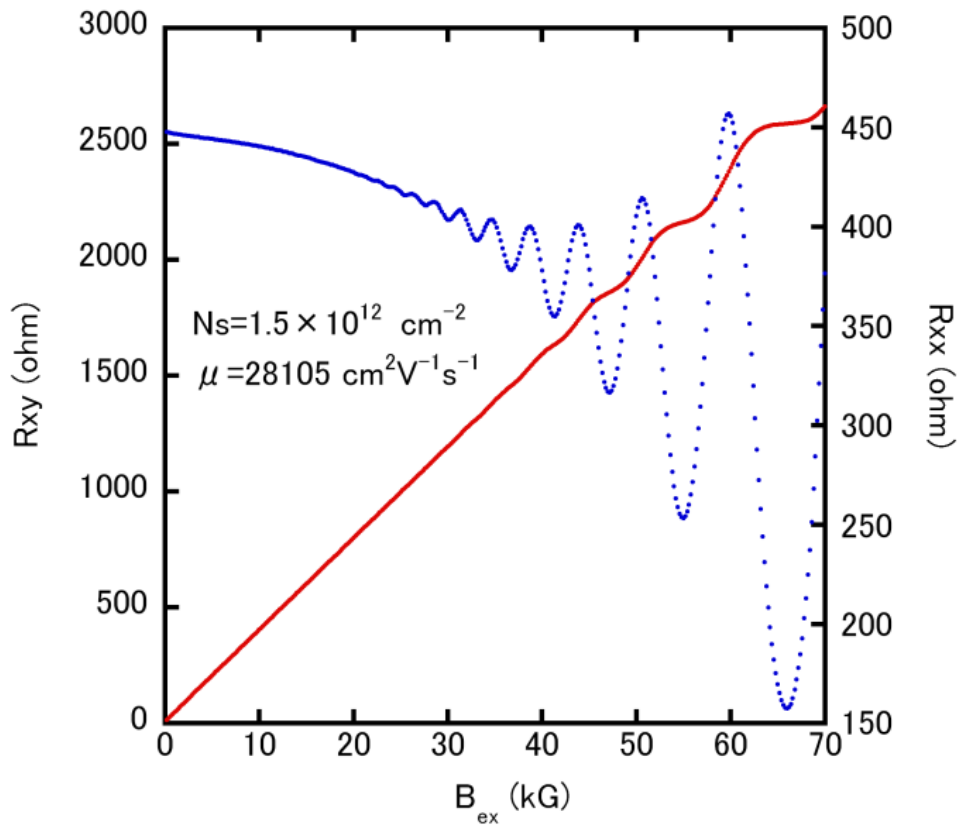


Figure 5.4.2. Quantum Hall effect and Shubnikov-de Haas oscillations in this samples of (110) direction at 1.5 K.

Mesa etching for the developed device isolation was established using conventional electron-beam lithography and wet chemical etching (phosphoric acid based etchant). As the source electrode, ferromagnetic metal was grown, which consisted with iron around 15 nm and Au 3 nm cap layer. The Fe electrode extends across the source edge of the mesa so that the contact from side edge is made possible, while drain electrode was stacked from top of mesa with Au/Ge/Pd alloys (Figure 5.4.3). This ferromagnetic electrode is designed in such a way that the injected spins are polarized perpendicular to the substrate, whose spin states are transmitted to the nuclear spins near the source edge through Overhauser effect, resulting in built-in magnetic field in out-of-plane direction.. When the current direction is opposite, i.e., electrons are injected from normal metal, the built-in magnetic field is expected to disappear. The present device structure is designed to verify the nuclear spin control by electron spin injection from the ferromagnetic electrode.

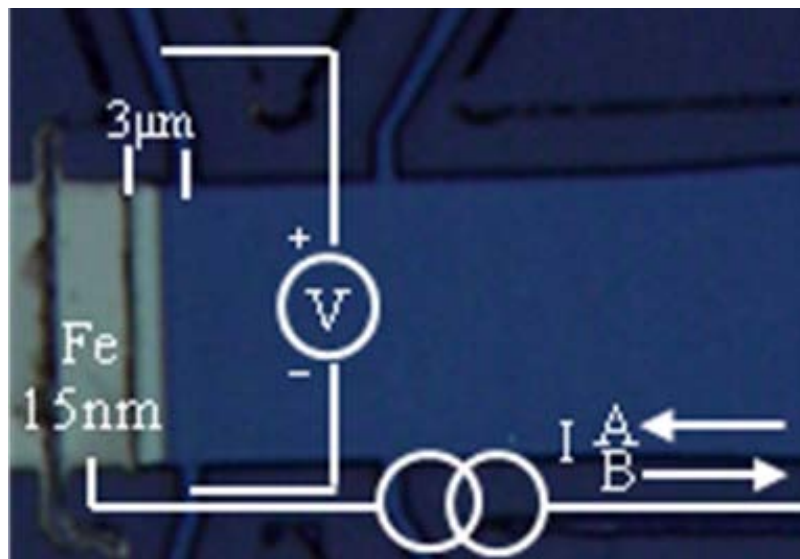


Figure 5.4.3 Optical microscopy image of the device. The drain electrode contacts the edge of mesa by 10 μm for injection of perpendicular polarized electrons spin.

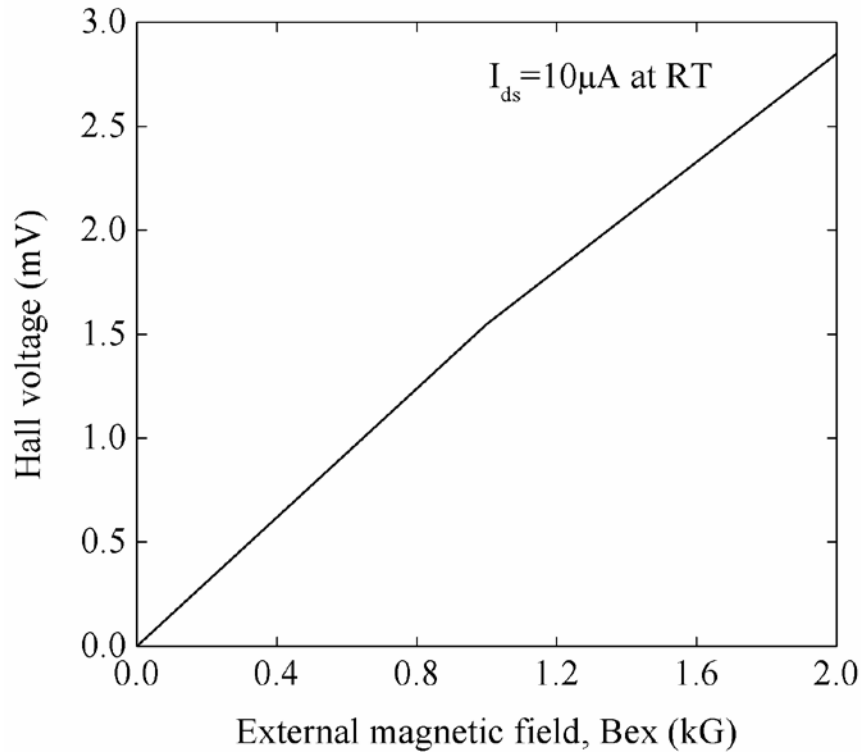


Figure 5.4.4. Conventional Hall measurement result was obtained at room temperature when the electron is injected from normal metal terminal.

5.4.2 Result and Discussions

Hall effect measurement is conducted by constant current from the normal metal (electrons are injected from ferromagnetic metal) under external magnetic field. This result is to be compared with the following measurement when steady spin current is supplied from the ferromagnetic electrode with remnant magnetization without external magnetic field. Fe electrode was magnetized in-plane, parallel to the current direction, yielding out-of-plane magnetization at the edge of the mesa step as shown in Fig. 5.4.5. Then, Hall measurement was carried out in zero external magnetic field in two current directions. Substantial Hall voltage was observed as shown in Fig. 5.4.6 (solid circle) in the case of electron injection from ferromagnet and much reduced negative Hall voltage was observed open circle) in the case of opposite current direction. The Hall voltage difference is too large to explain with the lithography pattern size variations between the relative Hall terminals. Possible explanation is nuclear magnetization near the spin injection edge (source) through spin exchange process between electron spin and the

nuclear spin (mostly contribution from indium atoms).

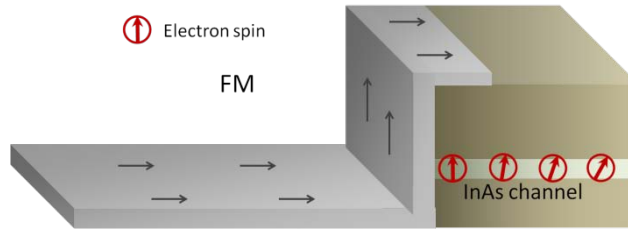


Figure 5.4.5 Schematic diagram of the Hall-device with Ferromagnetic electrode on InAs inverted heterostructure. The magnetization of the vertical source edge portion is intended to be magnetized with out-of-plane spin momentum.

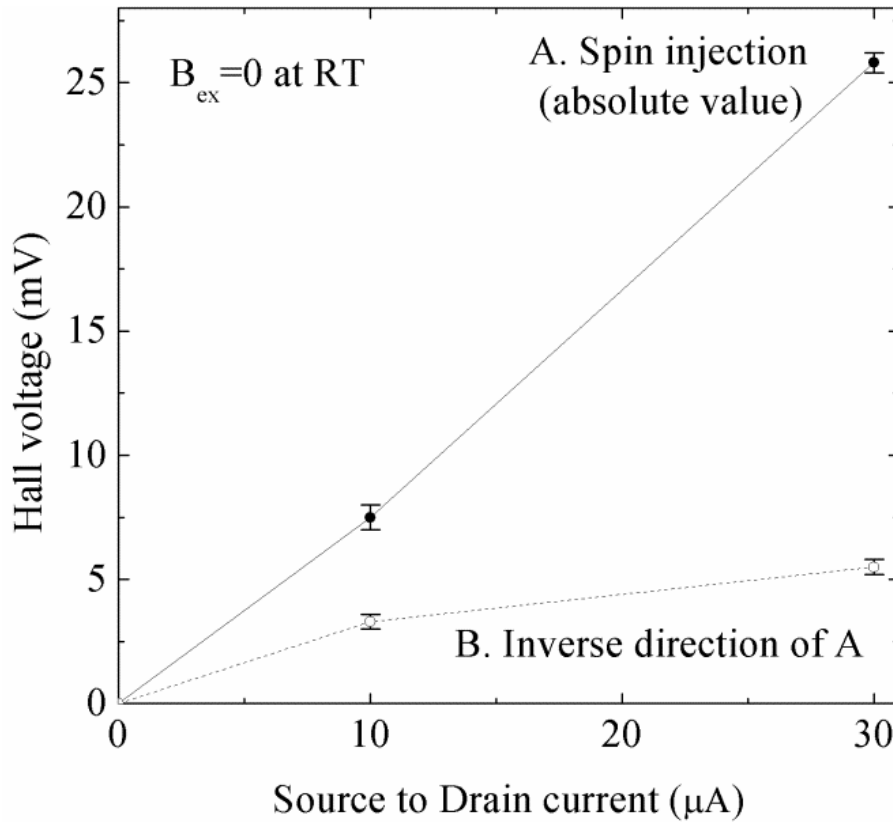


Figure 5.4.6 Hall voltage measurement in the absence of external magnetic field. Anomalous Hall voltage was observed when spin polarized electrons were injected from the ferromagnetic electrode (solid circle) when the Hall terminals at $3\mu\text{m}$ from the source edge. The Hall terminals at $8\mu\text{m}$ from the source edge hardly showed Hall voltage, suggesting local magnetic moment the channel.

The local nuclear magnetic field, when all nuclear spin aligned to same direction, is

described to $B_N = A \langle I_Z \rangle / (g^* \mu_B)$ is 15.5 kG in InAs two dimensional quantum well, where A is the hyperfine constant, $\langle I_Z \rangle$ is the quantum number of nuclear spin, g^* is the electron g-factor and μ_B is the Bohr magneton. [20-22] As the measurement result indicates approximately 3 mV of Hall voltage due to nuclear spin polarization by spin injection with 10 μ A, which corresponds to the local nuclear magnetic field ≈ 1 kG inferred from the conventional Hall measurement result shown in Fig. 5.4.3. Additional results in different sample (B), having small Fe/InAs contact length as one fifth of sample (A), did not show such anomalous Hall voltage with 3000 Gauss but finally similar abnormal Hall result after magnetization was observed with much higher external field (5T). Sample (B) result gives support to the present estimation. There was a sample (C) which did not show appreciable Hall voltage at room temperature with 3000 Gauss as sample (B), which was not subjected to magnetization with much higher field in order to cause vertical magnetization component at the mesa edge where spin injection takes place. Obviously successful perpendicular spin injection at the mesa edge depends on Fe thickness, mesa etching depth, ferromagnetic electrode pattern shape and magnetization field strength. The present anomalous Hall effect results suggest the possible nuclear spin control by magnetic electrode/InAs hybrid structures.

5.4.3 Conclusions

We have reported anomalous Hall voltage in an InAs channel Hall-bar structure with ferromagnetic spin injector in one of the current terminals. After magnetizing the Fe electrode, we have observed Hall voltage proportional to injected current when electrons are injected from the ferromagnetic terminal. This result suggests the possibility that out-of-plane spin injection from the channel edge lead to perpendicular nuclear magnetic field caused by nuclear spin polarization in InAs channel near the spin source edge through Overhauser effect. The estimated internal magnetic field of 2000 Gauss was inferred from the experiment which agreed reasonably well with the estimation with effectively 15 % of the nuclear spin magnetization in the channel.

Bibliography

- [1] Y. Kunihashi, T. Nihei, M. Kohda and J. Nitta, *Phys. Stat. Sol. C*, **5**, 322 (2008)
- [2] F. J. Ohkawa and Y. Uemira, *J. Phys. Soc. Jpn.*, **37**, 1325 (1974)
- [3] G. E. Marques and L. J. Sham, *Surf. Sci.*, **113**, 131 (1982)
- [4] T. Sasaki, T. Oikawa, M. Shiraishi, Y. Suzuki and K. Noguchi, *Appl. Phys. Lett.* **98**, 012508 (2011).
- [5] T. Uemura et al., *App. Phys. Lett.* **101**, 132411 (2012)
- [6] T. Suzuki, T. Sasaki, T. Oikawa, M. Shiraishi, Y. Suzuki and K. Noguchi, *Appl. Phys. Exp.* **4**, 023003 (2011)
- [7] H. C. Koo, J. H. Kwon, J. Eom, J. Chang, S. H. Han and M. Johnson, *Science* **325**, 1515 (2009).
- [8] J. Schliemann, J. C. Egues and D. Ross, *Phys. Rev. Lett.* **90**, 146801 (2003).
- [9] R. Winkler, *Phys. Rev. B* **69**, 045317 (2004).
- [10] T. Uemura, Y. Imai, M. Harada, K.-i. Matsuda, and M. Yamamoto, *Appl. Phys. Lett.*, **94**, 182502 (2009).
- [11] T. Uemura, M. Harada, K.-i. Matsuda, and M. Yamamoto, *Appl. Phys. Lett.*, **96**, 252106 (2010).
- [12] T. Uemura, M. Harada, T. Akiho, K. -i. Matsuda and M. Yamamoto, *Appl. Phys. Lett.* **98**, 102503 (2011).
- [13] T. Akiho, T. Uemura, M. Harada, K. -i. Matsuda and M. Yamamoto, *Appl. Phys. Lett.* **98**, 232109 (2011).
- [14] S. Takahashi and S. Maekawa, *Phys. Rev. B* **67**, 052409 (2003).
- [15] Sasaki, T. Oikawa, T. Suzuki, M. Shiraishi, Y. Suzuki, and K. Tagami, *Appl. Phys. Express* **2**, 053003 (2009).
- [16] A.W. Overhauser, *Phys. Rev.* **89**, 689 (1953).
- [17] K. Hashimoto et al, *Phys. Rev. Lett.* **88**, 176601 (2002).
- [18] C W Lai et al, *Phys. Rev. Lett.* **96**, 167403 (2006).
- [19] G. Yusa et al, *Nature* **434**, 1001 (2005).
- [20] D. Gammon et al, *Science* **277**, 85 (1997).
- [21] G. Salis et al, *Phys. Rev. B* **64**, 195304 (2001).

- [22]A. Fuhrer et al, Appl. Phys. Lett. 98, 202104 (2011).
- [23]D. Paget et al, Phys. Rev. B 15, 5780 (1977).
- [24]F. H. L. Koppens et al, Science 309, 1346 (2005).
- [25]P. -F. Braun et al. Phys. Rev. B 74, 245306 (2006).

Chapter 6

Summary of dissertation

This dissertation was described an experimental study for Datta-Das spin-FET. The initial work was about research for a thermally stable gate material on InAlAs barrier layer as substitute for conventional gate structures of Ti/Au and Ti/Pt/Au. These gate material diffusive to InAlAs Schottky layer around 200 °C, resulted to the gate characteristic deterioration. In addition, Ni and Fe as spin injector/detector are also easy to react with InAs at over 120 °C. In the reason, thermally stable gate material on InAlAs needed to be used for gate of spin FET. In Pd/InAlAs gate structure, there was no deterioration after thermal treatment at 250°C from analyzing the current-voltage characteristics and Hall-effect measurement.

The spin injection measurement was demonstrated in the lateral spin valves by using a Fe/n-Si and NiFe/MgO/n-Si for confirming a MgO tunneling barrier effectiveness. In nonlocal measurement, the NiFe/MgO/n-Si based lateral spin valves showed a clear nonlocal spin accumulation signals, while the Fe/n-Si did not show it. For further investigation of spin accumulation in the Fe/n-Si Schottky junction, the three-terminal-Hanle effect measurement was conducted. The results indicated that two kind of peaks cross over in single slope. It could be concluded that narrower Hanle peak originated from spin relaxation in n-Si. Because the extracted value of spin life time and the bias-dependent peak amplitude was similar to the results of nonlocal measurement. Moreover, NiFe/MgO/InAs and NiFe/InAs based lateral spin valve was fabricated as according to the NiFe/MgO/n-Si process. The nonlocal spin valve signal was clearly

shown and the spin injection efficiency reached to 9 %. This is the first trial for spin injection into InAs quantum well through MgO tunneling barrier. Finally, the nuclear polarization by spin injection in InAs quantum well was challenged. The anomalous Hall effect signals were detected when the spin is injected from ferromagnet injector. The Hall signal probably indicated the nuclear spin polarization in InAs QW.

List of Publications/Conferences

1. Publications related to this work

1. Tomotsugu Ishikura, Zhixin Cui, Takashi Matsuda and Kanji Yoh, “Thermal Stability of Pd Gate in Pseudomorphic InGaAs Heterostructures” Japanese journal of applied physics 50, pp06GF19-1, (2011)
2. Tomotsugu Ishikura, Lennart –Knud Liefeth, Zhixin Cui, Keita Konishi, Kanji Yoh and Tetsuya Uemura “Electrical spin injection from ferromagnet into an InAs quantum well through a MgO tunnel barrier” Applied physics express 7, 073001, (2014)

2. Publications related to other work

1. Tomotsugu Ishikura, Takahiro Hiraki, Takashi Matsuda, Joungeob Lee and Kanji Yoh “Nuclear spin polarization by out-of-plane spin injection from ferromagnet into an InAs heterostructure” Material research society fall meeting proceedings 1396, (2012)
2. Zhixin Cui, Tomotsugu Ishikura, Fauzia Jabeen, J –C. Hammand, Kanji Yoh “Fabrication and characterization of a d-dope InAs/InP core shell nanowire transistor” Journal of crystal growth 378, 511 (2013)
3. Zhixin Cui, Rajagembu Perumal, Tomotsugu Ishikura, Keita Konishi, Kanji Yoh, Junichi Motohisa “Characterizing the electron transport properties of a single <110> InAs nanowire” Applied physics express 7, 085001 (2014)

3. Presentation related to this work

International Conferences

1. Tomotsugu Ishikura, Zhixin Cui, Takashi Matsuda and Kanji Yoh “”Electrical Characterization of Pd Gate InAs-based Heterostructure” Microprocess and Nanotechnology Conference (MNC 2010), Kokura, Japan (November 2010)
2. Tomotsugu Ishikura, Zhixin Cui, Keita Konishi, Takashi Matsuda and Kanji Yoh “Electrical detection of nuclear polarization by the injection of out-of-plane polarized electrons into an InAs heterostructures” 5th International Workshop on Spin Currents (IWSC), p2-20, Sendai, Japan (July 2011)
3. Tomotsugu Ishikura, Zhixin Cui, Takahiro Hiraki, Takashi Matsuda, Joungob Lee and Kanji Yoh “Nuclear spin polarization by out-of-plane spin injection from ferromagnet into an InAs heterostructure” Material Research Society Fall meeting (MRS), Boston, USA, (December 2011)
4. Tomotsugu Ishikura and Kanji Yoh “Electrical Control of Nuclear-Spin-Induced Hall Voltage in an Inverted InAs Heterostructure“, Device Research Conference (DRC), III-41, Pennsylvania, USA (June 2012)
5. Tomotsugu Ishikura and Kanji Yoh “Electrical detection of nuclear spin polarization by out-of-plane spin injection from ferromagnet into an InAs heterostructure”, 31st International conference of the physics of semiconductor (ICPS), 36.15, Zurich, Switzerland (July 2012)
6. Tomotsugu Ishikura, Zhixin Cui, Keita Konishi, Joungob Lee and Kanji Yoh “Bias dependence of spin accumulation in Fe/n+-Si interface”, The 17th International Conference on Molecular Beam Epitaxy (MBE 2012), MoP-55, Nara, Japan (September, 2012)

7. Tomotsugu Ishikura, Zhixin Cui, Keita Konishi, Joungeob Lee and Kanji Yoh “Spin accumulation at the Fe/Si interface and two types of Hanle characteristics ”, 20th International Conference on Electronic Properties of Two-Dimensional Systems (EP2DS 20), MoP96, Wroclow, Poland (July, 2013)
8. Tomotsugu Ishikura, Zhixin Cui and Kanji Yoh “Enhanced spin injection by thermal anneal in NiFe/MgO/n-Si spin valve”, The 18th International Conference on Electron Dynamics in Semiconductors, Optoelectronics and Nanostructures (EDISON 18), TuP-22, Matsue, Japan (July, 2013)
9. Tomotsugu Ishikura and Kanji Yoh, “Spin injection enhancement in ferromagnet/InAs spin valves by interface resistance control” Seventh international school and conference on Spintronics and quantum information technology (Spintech 7), D03, Chicago, USA (July, 2013)
10. Tomotsugu Ishikura, Zhixin Cui, Keita Konishi, Kanji Yoh and Tetsuya Uemura “Enhanced spin injection from ferromagnet into InAs through MgO tunnel barrier”, The 6th IEEE International Nanoelectronics Conference (INEC 2014), INEC0095-SD, Sapporo, Japan (July, 2014)

Domestic Conferences (Japan)

1. 石倉 丈継, 陽 完治 「InAsシュードモルフィックヘテロ構造におけるスピンの注入による核スピン制御の電氣的検出」, 秋季第 72 回応用物理学学術講演会, 山形, 1a-S-14, 2011
2. 石倉 丈継, 陽 完治 「InAsヘテロ構造へのスピン注入」, 春季第 73 回応用物理学学術講演会, 17a-DP1-11, 東京, 2012
3. 石倉 丈継, 崔 志欣, 陽 完治, 「FM/InAsヘテロ構造におけるスピンの注入の非局所検出」, 2012 年秋季第 73 回応用物理学学術講演会, 愛媛, 11p-PA-6, 2012
4. 石倉 丈継, Lennart-Knud Liefeth, 崔 志欣, 小西 啓太, 陽 完治 「NiFe/MgO から InAs 量子井戸構造におけるスピンの注入の高効率化」, 春季第 60 回応用物理学関係連合講演会, 神奈川, 27p-PB2-1, 2013